Global and Planetary Change
July 2021, Volume 202, Pages 103526 (13p.)
https://doi.org/10.1016/j.gloplacha.2021.103526
https://archimer.ifremer.fr/doc/00696/80832/

Antarctic Polar Front migrations in the Kerguelen Plateau region, Southern Ocean, over the past 360 kyrs

Civel-Mazens M. [1, 2, *], Crosta X. [3], Cortese G. [4], Michel E. [5], Mazaud A. [5], Ther O. [3], Ikehara M. [1, 6], Itaki T. [2]

[1] Graduate School of Integrated Arts and Sciences, Kochi University, Japan
[2] Geological Survey of Japan (AIST), Tsukuba, Japan
[3] Université de Bordeaux, CNRS, EPHE, UMR 5805 EPOC, Pessac, France
[4] GNS Science, Lower Hutt, New Zealand
[5] Laboratoire des Sciences du Climat et de l'Environnement (LSCE), Gif-sur-Yvette, France
[6] Center for Advanced Marine Core Research, Kochi University, Japan

* Corresponding author : M. Civel-Mazens, email address : civelmatthieu@hotmail.fr

Abstract :

In the Southern Ocean (SO), climate-driven latitudinal migrations of the Antarctic Circumpolar Current (ACC) frontal system impact large-scale ocean circulation and primary productivity. Latitudinal migrations may not have been identical in all SO basins due to the presence or absence of regional bathymetric obstacles. The Antarctic Polar Front (APF), defined by the 3–5 °C surface temperature range and the 2 °C subsurface temperature minimum at 200 m, is particularly important for nutrient redistribution and biodiversity, influencing the soft tissue carbon pump in the modern SO. However, previous assessments of its migrations in the past, mostly based on a single metric or indirect observations, were not always robust. Here, we combine a new proxy for subsurface temperature (sub-ST) reconstructions based on radiolarian assemblages (sub-STrad), with relative abundance variations of key radiolarian species, and sea-surface temperatures (SST) reconstructions, based on diatom assemblages (SSTdiat), to refine estimations of the past mean APF locations in the Kerguelen Plateau (KP) region. Data from three sediment cores on a south (55°S) to north (47°S) transect are used to trace the mean APF locations for three climate states, glacials, peak-interglacials and mild-interglacials. Our results suggest that the APF, presently located south of Kerguelen Islands, shifted by 6–7 degrees of latitude and was located north of the KP during all glacial periods of the last 360 kyrs. This suggests that the ACC major flow interacted less with the bottom topography relative to its modern counterpart, probably resulting in less mixing of the water column over and in the lee of the KP. We propose that this process participated in the isolation of Antarctic surface waters (AASW) and in the reduction of macro-nutrient supply, thus resulting in lower regional productivity. During the warmer-than-present early interglacial periods, the APF probably migrated south by ~5 degrees of latitude relative to its modern position, to pass through the Fawn Trough. Contrary to glacial periods, the APF was forced in an “S” shape while the ACC main flow was constrained against the northern tip of the KP. In this configuration, a stronger interaction between the ACC, its associated fronts, and topography is expected, resulting in more mixing of the water column over and east of the KP. Congruently, siliceous productivity was probably restrained to latitudes south of the Fawn Trough.

Highlights

► New approach to estimate Southern Ocean fronts migrations in the past. ► Comparison of sea-surface and subsurface temperature records over the last 360 kyrs. ► APF positioned north of the Kerguelen Plateau during glacials. ► APF located in the Fawn Trough during early warm interglacials. ► Potential impact of ACC and associated fronts shifts on water column mixing.

Keywords : Southern Ocean, Fronts, Kerguelen, Radiolarians, Diatoms

1. Introduction

The Antarctic Circumpolar Current (ACC), driven by the westerly winds, is the dominant zonal flow in the Southern Ocean (SO). It is divided by a set of branching hydrological fronts, representing specific water mass boundaries and associated with merging and diverging jet currents (Orsi et al., 1995; Belkin and Gordon, 1996; Rintoul, 2001; Rintoul and Naveira Garabato, 2013). On a north to south transect, the main ACC fronts are the Subantarctic Front (SAF), the Antarctic Polar Front (APF) and the Southern-ACC Front (SACCF) (Figure 1). The Polar Front Zone (PFZ), encompassed by the SAF and APF, is particularly important for SO biogeochemistry and ecosystems as it separates colder, nutrient-richer (Si, NO_3^-) Antarctic Surface Waters (AASW), directly sourced from the SO upwelling, from warmer, nutrient-poorer Subantarctic surface waters (Ragueneau et al., 2000; Palter et al., 2013). As a result, diatoms represent the most abundant phytoplankton in the silicic acid-rich AASW, while coccolithophores dominate the silicic acid-poor Subantartic surface waters (Rigual-Hernández et al., 2015). Both diatoms and coccolithophores are important exporters of carbon to the SO depths (Tréguer and De la Rocha, 2013; Rigual-Hernández et al., 2020), with different impacts on atmospheric CO_2 drawdown. Indeed, it was shown that the dominance of diatoms

over coccolithophores in the glacial SO could have lowered atmospheric CO_2 by ~ 15 ppm (Matsumoto et al., 2002). The PFZ is also where AASW sink to mid-depth and form Antarctic Intermediate Waters (AAIW), a nutrient source to low latitude marine ecosystems (Sarmiento et al., 2004). Higher Si:N ratio in these waters during glacial times are supposed to have stimulated diatom production at low latitudes, which could account for an additional 10-15 ppm CO_2 drawdown (Matsumoto and Sarmiento, 2008; Matsumoto et al., 2014).

In the modern SO, regions where the ACC interacts with bathymetric obstacles represent a hot spot for upwelling and AAIW subduction (Langlais et al., 2017; Llort et al., 2017; Tamsitt et al., 2017; Klocker, 2018; Rintoul, 2018; Chapman et al., 2020). The Kerguelen Plateau (KP) represents the largest obstacle to the ACC in the Southern Indian Ocean (SIO) (Sokolov and Rintoul, 2009b; Park et al., 2014), dividing the ACC net flow into two main branches. As such, ~ 70 % of the ACC transport is concentrated north of the KP at 45°S, while the other ~ 30% is forced through the Fawn Trough at 56°S (Park et al., 2009). Additionally, the remobilisation of iron from KP sediments by the ACC induces massive diatom blooms that act as an important carbon sink (Blain et al., 2007; Graham et al., 2015). Latitudinal variations of the ACC, and of the APF in particular, have been shown to alter such iron remobilization (Kim et al., 2009), thus the regional productivity (Dezileau et al., 2003; Thöle et al., 2019) over the last glacial cycle and, potentially, CO_2 drawdown.

Over the past few decades, multiple studies have measured and located the modern APF through *in situ* sea surface temperatures (SST) measurements within a range of 2.5 – 4.1°C (Lutjeharms and Valentine, 1984), 4.1 – 5.7 °C (Belkin, 1989; Belkin and Gordon, 1996), 2.5 – 5.5 °C, identified with expendable bathymetry thermograph (XBT) probes and Conductivity Temperature Depth (CTD) devices (Anilkumar et al., 2006; Luis and Sudhakar, 2009); SST gradients of ~ 1.5 °C identified over a ~ 100 km distance in satellite data (Moore et al., 1999; Dong et al., 2006; Freeman and Lovenduski, 2016, Freeman et al., 2016); sea-surface height (SSH) single value contouring (Sokolov and Rintoul, 2002, 2007, 2009b; Gille, 2014; Kim and Orsi, 2014); or SSH gradients identification in satellite data (Graham et al., 2012; Chapman, 2014; Chapman, 2017). Although its identification is limited by the lack of high-resolution hydrographic data (Freeman and Lovenduski, 2016), the most robust APF definition is the northernmost extent of the 2 °C subsurface isotherm at 200 m water depth, also known as θ_{min} 2 °C (Botnikov, 1963; Park et al., 1993; Orsi et al., 1995; Belkin and Gordon, 1996; Park et al., 2014; Park et al., 2019).

Except SST, none of the aforementioned metrics can be reconstructed in the past. Ranges of SST, generally around 3 – 5 °C, were commonly used to approximate past APF positions from sediment archives (Dezileau et al., 2003; Gersonde et al., 2003; Bianchi et al., 2004; Bostock et al., 2013; Nair et al., 2019; Ghadi et al., 2020). Estimations of past APF migrations therefore remain elusive. We here combine diatom-based SST reconstructions (SSTdiat), radiolarian distribution and radiolarian-based sub-surface temperature reconstructions (sub-STrad), to provide a robust assessment of APF latitudinal shifts in the KP region over the last 360 kyrs.

Radiolarian are holoplanktonic protozoa (Suzuki and Not, 2015; Boltovskoy et al., 2017). In the Radiolaria phylum, only polycystines synthesize robust siliceous shells ($SiOH_4$) that are well preserved in sediments (Suzuki and Not, 2015; Boltovskoy et al., 2017). As their species assemblages vary according to water temperatures (Hays et al., 1976; Abelmann et al., 1999; Matul and Mohan, 2017), polycystine radiolarians were successfully used to estimate past temperatures (Hays et al., 1976; Abelmann et al., 1999; Cortese and Abelmann, 2002; Lüer et al., 2009; Panitz et al., 2015; Matsuzaki and Itaki, 2017; Matul and Mohan, 2017; Matsuzaki et al., 2019; Hernández-Almeida et al., 2020). In the SO, radiolarian mostly dwell in the subsurface layer, with their absolute abundance maximum occurring at ~ 100 – 400 m water depth (Abelmann and Gowing, 1997; Boltovskoy 1998, 2017). Most of their annual production occurs during Austral summer (Abelmann and Gersonde, 1991). As such, subsurface temperatures (sub-ST) at 200 m water depth are the best variable to explain radiolarian assemblage variance at high latitudes (Hernández-Almeida et al., 2020). Here, we make use of the particular ecological preferences of radiolarians and quantitatively reconstruct sub-STrad, in core MD11-3353 off Kerguelen Island in the SIO (Figure 1) in order to trace the θ_{min} 2 °C subsurface isotherm in the KP region over the last 360 kyrs. Additionally, a PCA is used to group co-varying species of radiolarian fossil assemblages preserved in core MD11-3353 and to associated them with the main ACC provinces, such as the Subantarctic Zone (SAZ), PFZ, or Antarctic Zone (AZ). These results are compared with SSTdiat and TEX_L^{86}-derived SST records from the same core along with published SSTdiat and sub-STrad records from other locations in the SIO. This allowed us to evaluate the mean APF positions during three different climate states, specifically glacials, peak-Interglacials (pIGs) and mild-Interglacials (mIGs) over the last 360 kyrs. Glacial and pIG periods document strongly contrasted conditions and benchmarks for paleoclimate models. Additionally, pIGs may give information on regional oceanographic conditions prevailing in the next few decades as a

response to anthropogenic warming. The mIGs are believed to provide a picture of the mean climate baseline, without anthropogenic forcing, of the future warming.

*** Figure 1 ***

2. Regional and frontal settings

In the SIO, several Subantarctic plateaus and islands disrupt the ACC zonal flow: the largest one is the Kerguelen Plateau, which extends from 46 to 68°S between 62 and 85°E and acts as a major topographic obstacle. It causes the main ACC flow (~ 150 Sv) to separate into two main branches and several lesser currents (Belkin and Gordon, 1996; Park et al., 2009; Sokolov and Rintoul, 2009b; Park et al., 2014). Based on several studies (Park et al., 2008; Park et al. 2009; Park et al., 2014; Park et al., 2019), the intricate ACC branching over the KP region can be summarized as follows: the northern branch of the ACC, representing ~ 70% of the net flow (~ 90 Sv), is associated with the SAF (Park et al., 2008; Park et al., 2014), passing north of the KP at ~ 45 °S (Figure 1 – red line). The SAF separates the SAZ surface waters to the north from the PFZ surface waters to the south and is identified by θ_{min} 6 – 5 °C at 200 – 400 m in the SIO (Belkin and Gordon, 1996; Park et al., 2019). The SACCF corresponds to the southern limit of the Upper Circumpolar Deep Water (UCDW), and is identified by θ_{min} 0 °C at 200 m in the SIO (Belkin and Gordon, 1996; Park et al., 2019). In the KP region, it is associated with the majority (~ 43 Sv) of the southern ACC branch and passes through the Fawn Trough (Figure 1 – black line), a 2600 m deep sill splitting the KP in two at ~ 56 °S (Roquet et al., 2009; Park et al., 2009). Between the SAF and SACCF, the APF separates the PFZ surface waters to the north from the AASW to the south. Over the KP, the APF represents a flow of 2 Sv (Park et al., 2014; Pauthenet et al., 2018), rounding the Kerguelen Islands (KI) to the south at ~ 51 – 52°S. The APF then flows northward immediately after the KI until ~ 47 °S before turning back south-eastward downstream of the KP (Figure 1, blue line). Despite its transport being volumetrically low, the APF represents an important physical barrier separating two chlorophyll plumes observed east of the KI region (Park et al., 2014).

3. Material & Methods

3.1 MD11-3353 core description, sampling and age model

Core MD11-3353 (50°34.02'S - 68°23.13'E, 1568 m water depth), was collected with a CALYPSO piston corer during the oceanographic expedition MD185 INDIEN-SUD-1 on board of the R/V Marion Dufresne II (Mazaud and Michel, 2011). The core site is located west of KI in the PFZ, near the APF (Figure 1). The core is 38.51 meters long and covers ~ 360 kyrs with an average sedimentation rate of 10 cm/kyr. The sediment is composed of homogenous diatom ooze mixed with calcareous silts in sections covering warmer periods. Core MD11-3353 age model was built by correlating its temperature records with the δD record of the well-dated EPICA Dome C (EDC) ice core (Jouzel et al., 2007; Bazin et al., 2013), with the assumption that southern high latitude air and ocean temperatures varied synchronously through time (Govin et al., 2015). Its TEX_L^{86} SST record was used for the first 1150 cm of the core (Figure 2), covering the last ~ 140 kyrs (Thöle et al., 2019). Beyond the TEX_L^{86} SST record, the radiolarian based subsurface temperature record (this study) was tuned to EDC δD record (Figure 2), which provided 37 additional tie-points (Figure 2 and supplementary material 1).

*** Figure 2 ***

3.2 Radiolarian microscopic slides and counts

Microscopic slides were prepared according to Itaki et al. (2018). Radiolarian identification was performed on a Zeiss Imager A2 microscope at a ×100 magnification and follow taxonomic rules described in previous studies using radiolarians for environmental reconstructions in the SO (e.g., Cortese and Abelmann, 2002; Panitz et al., 2015). Radiolarian identification was performed in 470 samples taken from the first 36 m of core MD11-3353 in order to reconstruct past summer (JFM) sub-STrad with a mean temporal resolution of 800 years. A sample every 10 cm (~ 1000 – 1500 years) and a sample every 2 – 4 cm (~ 200 – 600 years) were taken for stadial climates and deglaciations, respectively. An average of 356 (min. 301; max. 469) radiolarian specimens per sample were identified. In core MD11-3353, the 81 radiolarian species selected for the transfer function represented an average of 94% (min. 85.9%, max. 99.7%) of the total assemblages preserved downcore.

3.3 PCA and sub-STrad

A Principal Component Analysis (PCA) was applied to the radiolarian relative abundances of core MD11-3353 using PAST v4.03 software (Hammer et al., 2001) in order to identify and group species presenting similar down-core variations. Three main groups were recognized by the PCA, and, for each group, variations in relative abundances of species with factor loadings > 0.2 were interpreted. We assessed changes in the prevalent ACC province (e.g., PFZ, SAZ, AZ) at the MD11-3353 core site for a given climate state from variations in relative abundances and known ecology preferences of these species. The modern radiolarian reference database includes 209 surface sediment samples (modern analogs) distributed in the three sectors of the SO (Lawler et al., submitted). Among these 209 surface sediment samples, two samples with less than 100 counted specimens were removed. An average of 396 radiolarians were counted in the 207 samples composing the training dataset (min. 101; max. 706). Eighty-one radiolarian taxa presented relative abundances > 2% in at least one station and were used for subsequent statistical analyses (Imbrie and Kipp, 1971). These taxa account for an average of 68.3% (min. 25%, max. 94.8%) of the training dataset assemblages. Summer sub-ST (JFM, 200 m) were extracted from the World Ocean Atlas (WOA, Locarnini et al., 2013) at each surface sediment location on a 0.25 x 0.25° grid. The sub-STrad in core MD11-3353 were calculated by applying the Modern Analog Technique (MAT) to the radiolarian relative abundances (Prell, 1985) with the PaleoAnalogs free software (Therón et al., 2003). The square-chord distance and weighting of averages settings were used to predict past temperatures by selecting the ten most similar modern analogs. This method yielded a r^2 of 0.97, a RMSEP of ± 1.2 °C and an average standard deviation of ± 1.5, over a range of -1 to 21 °C.

3.4 Diatom microscopic slides and counts

Diatoms are present in both oceanic and freshwater environments, and in the SO they peak in abundance around 0 – 100 m water depth (DiTullio et al., 2003). For this study, diatom census data were produced for 131 samples from core MD11-3353, in order to reconstruct summer sea-surface temperatures (SSTdiat). Microscopic slides were prepared at EPOC (Bordeaux, France), according to the laboratory standard protocol for diatom slide preparation (Crosta et al., 2020). Diatom census counts were performed on a Nikon ECLIPSE 80i microscope at a

×1000 magnification, at a sample spacing of 10 cm from 0 to 1300 cm in core MD11-3353 (resolution of ~ 1000 – 1500 years). A minimum of 300 diatom valves were counted in each sample, following the species identification criteria detailed by Crosta et al. (2020). The 32 diatom species selected for the transfer function represented an average of 88.3% (min. 69.8%, max. 97.8%) of the total assemblages preserved downcore.

3.5 SSTdiat

MAT was applied to the relative abundances of diatoms to reconstruct past summer SSTdiat (JFM) in core MD11-3353, and was run via the "bioindic" R package (Guiot and de Vernal, 2011). The modern reference database includes 249 surface sediment samples (modern analogs), in which a minimum of 300 diatoms were counted (Crosta et al., 2020), and for whose locations modern summer SST were interpolated on a 1° x 1° grid from the World Ocean Atlas (WOA13, Locarnini et al., 2013) through Ocean Data View (Schlitzer, 2002). We used the relative abundances of 32 diatom species and the chord distance to select the five most similar modern analogs. The threshold dissimilarity criterion is fixed at the first quartile of random distances on the modern dataset. This method yields a r^2 of 0.96 and a RMSEP of ± 0.96 °C for summer SST over a range from -2 to 22 °C. The 32 taxa account for an average of 93% (min. 47.2%, max. 100%) of the training dataset assemblages. More details can be found in Crosta et al. (2020).

4. Results

4.1 Species relative abundances

A PCA was applied to all samples of core MD11-3353 in order to identify groups of radiolarian species whose relative abundance co-varied through time. Only species with factor loadings > 0.2 are considered here. The first three PCs (PC1, PC2 and PC3) account for 90% of the data variance. In PC1 (61% of variance), the *Antarctissa* group (*Antarctissa* spp., *A. denticulata*, and *A. strelkovi*) displays the highest positive factor loadings, while *Cycladophora davisiana* obtained the highest negative values (Table 1). PC2 (24% of variance) is positively driven by *Antarctissa* gp and *C. davisiana* and is negatively driven by the *Lithomelissa setosa* group (*L. setosa*, *L. hystrix*, *Trisulcus testudus*) and by *Cycladophora*

bicornis (Table 1). PC3 (5% variance) is positively driven by *L. setosa* gp and *C. bicornis* and negatively by *Lithomelissa* sp. A, *Botryostrobus auritus/australis* (thereafter *Botryostrobus auritus*), and *Pseudodictyophimus gracilipes* group (*Dictyophimus bicornis, P. gracilipes, P. platycephalus*; Table 1). Factor loadings for all 81 species are provided in supplementary material 2 and relative abundance changes of the 7 taxa highlighted above are shown in Figure 3.

*** Table 1 ***

In core MD11-3353, the *Antarctissa* gp has an average abundance of 46%, which generally increase during the coldest parts of interglacials or warmest parts of glacials, while they generally decrease during full glacials or interglacials (Figure 3G). In the modern ocean, it thrives at ~ 100 – 200 m in 2 °C waters with high dissolved silica concentrations in the Permanent Open Ocean Zone (POOZ) of the South Atlantic (Abelmann and Gowing, 1997), which corresponds to the northern extent of AZ or the APF (Figure 3G). *Cycladophora bicornis* and the *L. setosa* gp generally show relative abundances below 3% in core MD11-3353. Their relative abundances increase during interglacial periods (Figure 3H-I), especially during the Holocene when *C. bicornis* and *L. setosa* gp account for ~ 16% and ~ 30% of the assemblage, respectively. In the South Atlantic, they live at ~ 100 – 400 m and ~ 50 – 400 m water depths, respectively (Abelmann and Gowing, 1997; Boltovskoy, 2017). As *C. bicornis* was previously associated with the Northern PFZ – SAZ (Abelmann and Gowing, 1997), and as both taxa are negatively driven PC2 and are positively correlated to PC3, they are associated with the SAZ (Figure 3H-I). The relative abundances of *Pseudodictyophimus gracilipes* gp (average of 3%), *B. auritus* (average of 4%), and *Lithomelissa* sp. A (average of 8%), generally increase during glacial periods, particularly during the MIS 8 and MIS 6. Conversely, their relative abundances decrease across deglaciations to reach lower values during the early interglacial periods (Figure 3D-F). *Botryostrobus auritus* and *P. gracilipes* gp live at ~100 – 400 m water depths in the South Atlantic (Boltovskoy, 2017). They are both anticorrelated to PC3 and *P. gracilipes* gp was previously associated with the AZ, in the South Atlantic POOZ (Abelmann and Gowing, 1997). Both taxa are, thus, associated to the AZ in the KP region (Figure 3D-E). According to Abelmann and Gowing (1997), *Lithomelissa* sp. A lives in the AZ at 400 – 1000 m water depth. In core MD11-3353, *Lithomelissa* sp. A co-varies with *B. auritus* and *P. gracilipes* (Figure 3D-F) and all three are negatively correlated to PC3. Therefore, we associate it to the AZ. *Cycladophora davisiana* have average relative abundances of 9%, reaching higher values during glacial periods,

similar to *B. auritus*, *Lithomelissa* sp. A and *P. gracilipes* gp. Its maximum abundance (52 %) occurs during the MIS 2 – 4 (Figure 3C). This species thrives at 200 – 600 m depths in intermediate water masses with overlying seasonal sea ice (Morley and Hays, 1983; Hays and Morley, 2003; Abelmann and Nimmergut, 2005; Abelmann et al., 2006; Itaki et al., 2009). In the SO, this description fits the intermediate layer in the glacial AZ (Hays and Morley, 2003; Abelmann et al., 2006). To complement these results, the downcore scores of three PCs are presented in supplementary material 3.

*** Figure 3 ***

4.2 SSTdiat and sub-STrad

In Civel-Mazens et al. (2021), we used the Imbrie and Kipp method (IKM) (Imbrie and Kipp, 1971) for sub-STrad calculation to enable a direct comparison of our results to previous SO studies (Abelmann et al., 1999; Cortese and Abelmann, 2002; Cortese et al., 2007; Panitz et al., 2015). However, MAT is the most commonly used statistical approach to quantitatively reconstruct SST from diatom assemblages (Crosta et al., 2004; Gersonde et al., 2005; Esper and Gersonde, 2014; Nair et al., 2019; Ghadi et al., 2020; Orme et al., 2020) and was recently used for radiolarian-based reconstructions (Hernández-Almeida et al., 2020). We therefore applied the same approach to radiolarian assemblages to ensure a more robust comparison of SSTdiat and sub-STrad in core MD11-3353.

Based on EDC ice core δD record (Jouzel et al., 2007; Bazin et al., 2013) the last four interglacials MIS 1, MIS 5.5, MIS 7.5 and MIS 9.3, unfolded in two phases. After each deglaciation, a short peak in temperatures (pIGs) occurred (red bars on Figure 3), and was followed by a plateau of milder temperatures (mIGs) (green bars on Figure 3). This delineation was used for our interpretations to document potential future climate conditions that will prevail in the KI region, based on the last four warmer-than-modern pIGs. Mild-interglacials are believed to provide a picture of the mean climate baseline, with no anthropogenic influence.

In core MD11-3353, sub-STrad display a mean of 2.1 °C, a minimum of 0.49 °C and a maximum of 4.2 °C over the past 360 kyrs (Figure 3A). Glacial periods (grey bars in Figure 3) showed generally cold temperatures of about ~ 1.5 °C: mean of 1.6 °C (0.49 – 2.8 °C) during the MIS 2 – 4 (18 – 70 kyrs); mean of 1.5 °C (0.49 – 2.3 °C) during the MIS 6 (138 – 198 kyrs); mean of 1.5 °C (0.7 – 2.8 °C) during the MIS 8 (250 – 310 kyrs); mean of 1.4 °C (0.6 – 1.9 °C) during the late MIS 10 (340 – 360 kyrs).

Mean temperatures over ~ 3 °C were recorded during pIGs: mean of 3.3 °C (3 – 3.95 °C) during the Holocene Climatic Optimum (HCO) (9 – 11.4 kyrs); mean of 3.7 °C (3.1 – 4.2 °C) during the pIG-5 (126 – 133 kyrs); mean of 3.1 °C (2.9 – 3.4 °C) during the pIG-7 (243 – 247 kyrs); mean of 3.5 °C (2.5 – 3.7 °C) during the pIG-9 (333 – 337 kyrs).

During mIGs, sub-STrad display temperatures of ~ 2.7 or 3.3 °C: mean of 2.8 °C (2.4 – 3.3 °C) during the Holocene (0 – 9 kyrs); mean of 3.3 °C (2.4 – 3.8 °C) during the mIG-5 (116 – 126 kyrs); mean of 2.7 °C (2.3 – 3 °C) during the mIG-7 (237 – 243 kyrs); mean of 3.4 °C (3.1 – 3.6 °C) during the mIG-9 (326 – 333 kyrs).

Diatoms in core MD11-3353 reconstruct a mean temperature of 3.4 °C oscillating between a minimum of 0.7 °C and a maximum of 8.8 °C over the last 150 kyrs (Figure 3B). SSTdiat display mean values of 5.5 °C (3.7 – 8.3 °C) during the Holocene; mean of 8 °C (7.4 – 8.5 °C) during the HCO; mean of 2.4 °C (0.8 – 6.1 °C) during the MIS 2 – 4; mean of 5 °C (3.4 – 7.3 °C) during the mIG-5; mean of 7.9 °C (6.6 – 8.8 °C) during the pIG-5; mean of 1.2 °C (0.8 – 2.2 °C) during the late MIS 6. Box and whiskers plots, for both for radiolarian- and diatom-derived temperatures during each period, are presented as visual support to summarize this information (Figure 4).

*** Figure 4 ***

5. Discussion

As previously observed in a 40 kyrs long record recovered east of KI (Civel-Mazens et al., 2021), the sub-STrad pattern in core MD11-3353 on a depth scale is exceptionally similar to the EDC ice core δD record (Thöle et al., 2019). Our new record extends this finding by three climate cycles (Figure 2). The close resemblance of our new sub-STrad record to EDC δD record therefore suggests that ocean subsurface temperature variations over the past 360 kyrs were controlled by climate and were robustly recorded by radiolarian assemblages. Radiolarian counts were performed at high resolution, improving confidence that mean temperatures accurately represent the prevailing mean climate states during the selected

periods. In the following sections, we use new SSTdiat and sub-STrad along with published sub-STrad, TEX_L^{86} SST and SSTdiat regional records to reconstruct the mean location of the hydrological fronts, mainly the APF, in the KI region during glacial and interglacial periods. We based our inferences on two hypotheses. First, we assumed that the θ_{min} 2 °C at 200 m defined the APF in the past like it does in the modern ocean, despite reorganization of water masses in the SO due to climate variations. Second, we assumed that gradients in sub-surface isotherms did not drastically change in the past. Given these assumptions, past mean locations of the fronts were estimated in respect to regional modern conditions. Although the WOA of 2018 (WOA18) (Locarnini et al., 2019), a gridded atlas, is commonly used to infer large-scale modern conditions, it may not be adapted to account for the dynamic oceanographic conditions off KI. Indeed, the WOA18 suggests modern summer sub-ST at 200 m of ~ 7 °C at the MD12-3396CQ core site (87°E) whereas the nearby (90°E) high resolution eWOCE leg I8 survey (Schlitzer, 2000; Orsi and Whitworth, 2005) suggests summer sub-ST of ~ 5 – 6 °C. The difference between these two atlases downstream of the KP probably originate from mesoscale structures in this area, well resolved in the WOCE, but smoothed down in the WOA18. The sub-STrad reconstructed in the MD12-3396CQ core-top sample, dated at 592 years BP (Gottschalk et al. 2020), at ~ 4 °C is in better agreement with WOCE I8 than WOA18, indicating that radiolarians were probably impacted by these recurrent sub-surface mesoscale structures and recorded them. Moreover, TEX_L^{86} SST, SSTdiat and sub-STrad of 5.4 °C, 5.5 °C and 2.7 °C, respectively, reconstructed in the MD11-3353 core-top sample are, again, in better agreement with the eWOCE (station 74DI207; Schlitzer, 2000; WOCE, 2002), which displays warmer summer temperatures (5.3 °C at 10 m and 2.5 °C at 200 m) than WOA18 (~ 4 °C and ~ 2 °C) over the core site. Therefore, to avoid discrepancies with gridded atlases, we here chose to use the core-top temperatures as references for the modern ocean and we interpreted past conditions for the three selected climate states relative to these core-top temperature values. Accordingly, modern SST and sub-ST references at MD11-3353 core site are 5.5 °C and 2.7 °C, respectively. Based on sub-STrad, the modern sub-ST reference at the MD12-3396CQ core site is 4.4 °C.

*** Figure 5 ***

5.1 Glacial

In core MD11-3353, a mean sub-STrad of ~ 1.5 °C is reconstructed for each glacial over the last 360 kyrs (Figure 4; Figure 5D). This suggests that oceanographic subsurface conditions were rather similar during each glacial of the last 360 kyrs and were colder than modern

conditions by ~ 1 °C. In the modern ocean, the subsurface isotherm of 1.5 °C at 200 m is located 2° south of the θ_{min} 2 °C (APF) in the study area (Orsi and Whitworth, 2005; Locarnini et al., 2019). Therefore, we propose that the θ_{min} 2 °C, and thus the APF, were located at least 2° north of MD11-3353 core site during the last four glacials. The PCA results on radiolarian assemblages in core MD11-3353 allowed for the identification of three distinct groups of co-varying radiolarian taxa which live preferentially in AZ cold waters (Figure 3C-F), APF waters (Figure 3G) or SAZ warmer waters (Figure 3H-I). During glacials, the relative abundances of the four radiolarian taxa related to AZ realm increased, while abundances of the two taxa associated to the SAZ decreased below 2%. In the AZ group: *Cycladophora davisiana* reached its maximum abundance during the MIS 2 – 4, the *P. gracilipes* gp did so during the MIS 6 while *Lithomelissa sp. A* and *B. auritus* reached their maximum abundance during MIS 8. These results suggest a northward expansion of the AZ realm over the northern KP during all glacials, as already observed in the SO (Pichon et al., 1992; Pichon et al., 1998; Dezileau et al., 2003; Becquey and Gersonde, 2003; Gersonde et al., 2003; Bianchi et al., 2004; Gersonde et al., 2005; Katsuki et al., 2012; Bostock et al., 2013; Shetye et al., 2014; Nair et al., 2015; Benz et al., 2016). In core MD11-3353, mean SSTdiat were ~ 2.4 °C during the MIS 2 – 4 and ~ 1.2 °C during the late MIS 6 (Figure 4, Figure 5C), were similar to mean TEX_L^{86} SST of ~ 2 °C and ~ 1.6 °C, respectively (Thöle et al., 2019; Figure 5B). However, TEX_L^{86} and SSTdiat records do not encompass the full length of the MIS 6 and lack the warmer early glacial. Even so, glacial SST values were lower than modern conditions at the core site by ~ 3 °C and below the surface temperature range generally used to infer the position of the APF (~ 3 – 5 °C; Lutjeharms and Valentine, 1984; Anilkumar et al., 2006; Luis and Suhdakar, 2009). These concurrent results suggest that the APF was located north of the core site during the last four glacials. As the KP is a major obstacle to the ACC flow, we propose that such migration was amplified by the regional bathymetry, forcing the APF to round the KP to the north at ~ 45 – 46 °S. Hence, the mean APF was located ~ 6 – 7° north of its modern position (Figure 6A).

Downstream of the KP, the surface waters at the MD12-3396CQ core site (47°43'S and 86°41'E, east of KI) were influenced by lower latitudes warmth redistributed via the Agulhas Return Current (RC) to the SIO during the MIS 2 – 3 (Civel-Mazens et al., 2021). Contrary to the SSTdiat, sub-STrad in this core did not record the injection of low latitude warmth, which was limited to the surface layer of the ocean, and sub-STrad can, therefore, reliably trace the θ_{min} 2 °C. Mean sub-STrad were ~ 1.6 °C in core MD12-3396CQ during the MIS 2 – 3 period

(Figure 5A), indicating the subsurface to be ~ 3 °C cooler than modern conditions at the core site. It should be noted that the sub-STrad record in this core does not encompass the full length of the MIS 2 – 4 and, thus, does not cover the warmer early glacial. Even so, they support a northward shift of the APF. In the modern ocean and downstream of the KP, nearby the MD12-3396CQ core site, the 1.6 °C subsurface isotherm at 200 m is located ~ 1 – 2° south of θ_{min} 2 °C. This suggests that the θ_{min} 2 °C, and the APF, shifted a couple of degrees to the north of the core site during the MIS 2 – 4 and, thus, ~ 4 – 5° north of its current position downstream of the KP (Figure 6A). These results suggest a more zonal APF and ACC main flow. As a result, the ACC northern branch was probably not as tightly constrained against the northern KP as it is today. This indicates weaker interactions between the main ACC fronts and the regional bathymetry during last four glacials as compared to modern conditions.

Recently, Ghadi et al. (2020) used their SSTdiat record from a core located south of Conrad Rise (45°E), and the SACCF SST range of 1 – 2 °C (Sokolov and Rintoul, 2009a), to infer a ~ 3° of latitude northward migration of this front to settle at ~ 55°S during the last two glacials. Using the same criterion, we propose that mean SSTdiat of ~ 1 °C in core MD84-551 (55°S – 75°E; Figure 1), during the MIS 2 – 4 and MIS 6 (Pichon et al., 1992; Figure 5E; updated age model in supplementary material 4) indicate that the SACCF shifted close to this core site, probably to sit in the Fawn Trough at 56°S. The SACCF was therefore located ~ 2 – 3° to the north of its modern position (Figure 6A) consistent with Ghadi et al. (2020) interpretations.

5.2 Interglacials

Peak-interglacials (pIGs)

Mean sub-STrad over 3 °C in core MD11-3353 for all pIGs of the past 360 kyrs (Figure 4; Figure 5D) indicate the occurrence of warmer-than-modern conditions in the modern KP region by ~ 0.5 – 1 °C during the climate optima. In the modern ocean, the subsurface isotherm of 3 °C at 200 m is located north of the KP at ~ 45 °S, around 5 – 6° of latitude north of the θ_{min} 2 °C (Orsi and Whitworth, 2005; Locarnini et al., 2019). This suggests the APF migrated by ~ 5° of latitude to the south during the last four pIGs. Moreover, during all pIGs, the AZ-related radiolarian species in core MD11-3353 decreased in relative abundances (Figure 3C-F) whereas the relative abundances of the two radiolarian taxa (*C. bicornis* and *L. setosa* gp) affiliated with SAZ warmer-water environments increased (Figure 3H-I). These results point to a southward expansion of the SAZ and PFZ, supporting that the APF shifted south of its modern position. In this same core, mean SSTdiat of ~ 8 °C reconstructed for the

HCO and pIG-5 (Figure 4; Figure 5C) were similar to TEX_L^{86} SST of 7.6 °C during the HCO but ~1.5 °C lower than the mean TEX_L^{86}SST during pIG-5 (Figure 5B). Nevertheless, all pIGs SST values in core MD11-3353 were ~ 2 – 4 °C above the core–top SST reference and the modern APF SST range. This further hints at a large latitudinal shift of the APF over the last two pIGs, in good agreement with sub-STrad in the same core. So where was sitting the APF during the pIGs, considering the large obstacle that is the KP to the ACC flow? Mean SSTdiat of ~ 5.6 °C were reconstructed for the HCO and pIG-5 in core MD84-551 (Figure 5E), slightly above the modern APF SST range, suggesting the close proximity of the APF. Results in cores MD11-3353 and MD84-551 together, suggest that the APF was forced by the KP's topography to its southernmost position during the last four pIGs, reaching the Fawn Trough at around 55 – 56 °S (Figure 6B).

The mean sub-STrad of ~ 6.2 °C in core MD12-3396CQ indicates that subsurface temperatures were ~ 2 °C higher during the HCO than today (Figure 5A). Although this value is too high to realistically track θ_{min} 2°C, it suggests that the mean APF, east of KI, was located south of its modern position during the HCO. In the modern ocean, the 6 °C isotherm lies ~ 3-4 degrees of latitude north of the 2 °C isotherm (Orsi and Whitworth, 2005; Locarnini et al., 2019), which may indicate a similar southward migration of the APF east of KI during the pIGs. If true, the APF turned to the north downstream of the Fawn Trough, probably following the plateau's eastern flank as bottom-pressure torque forces the flow equatorward when topography rapidly deepens (Rintoul, 2018), before turning again to the east forcing the flow into a pronounced "S" shape east of KI (Figure 6B). Additional cores downstream of the Fawn Trough are required to confirm the position and shape of the APF during pIGs.

Mean sub-STrad < 4 °C during all pIGs in core MD11-3353 (Figure 4, Figure 5D) indicate that the SAF (modern θ_{min} 6 – 5 °C at 200 – 400 m), and its associated transport, were still passing north of the KP over the last four pIGs. Downstream of the KP, the aforementioned mean sub-STrad of ~ 6.2 °C in core MD12-3396CQ during the HCO (Figure 5A), were 2 °C warmer-than-modern subsurface temperatures at the core site. In the modern ocean, the 4 to 8 °C sub-ST contours east of KI are, however, tightly constrained in a 2 degrees latitudinal range, indicating that the SAF was probably located slightly to the south of its modern position. In that configuration, greater front/bathymetry interactions, compared to glacials, are expected.

Mild-interglacials (mIGs)

The sub-STrad record in core MD11-3353 depicts two different situations during the mIGs, following pIGs' climate optima, over the past 360 kyrs. During mIG-5 and mIG-9, subsequent to the stronger pIGs, pIG-5 and pIG-9, respectively, mean sub-STrad were over 3 °C (Figure 4, Figure 5D). Conversely, during the Holocene and mIG-7 subsequent to the weaker pIGs, HCO and pIG-7, respectively, mean sub-STrad were of ~ 2.7 °C (Figure 4, Figure 5D).

In core MD11-3353, mean sub-STrad of ~ 3.3 °C were reconstructed for mIG-5 and mIG-9. These values are comparable to the ones observed during each pIG (mean sub-STrad of 3.1 – 3.7 °C during pIGs, Figure 4), which suggests that the APF was still located at the Fawn Trough after the two corresponding climate optima (pIG-5 and pIG-9). Supporting this hypothesis, the SAZ-related radiolarian taxa showed similar relative abundances during the mIG-5 and mIG-9 and during pIG-5 and pIG-9 (Figure 3H-I). In core MD11-3353, mean SSTdiat of ~ 5 °C and mean TEX_L^{86} SST of ~ 6 °C during mIG-5 (Figure 4, Figure 5B-C), above the APF SST range (3 – 5 °C), tend to agree with the radiolarian-based results, indicating that the APF was indeed south of the core site. Moreover, mean SSTdiat of ~ 5 °C during the mIG-5 in core MD84-551 (Figure 5F), above the APF SST range, indicates that the APF passed through the Fawn Trough during the mIG-5. As such, we propose that the mIG-5 and mIG-9 oceanographic configuration was similar to the one described for pIGs in the previous section and that the APF was locked in the Fawn Trough for over 10 kyrs during stronger interglacials.

In core MD11-3353, mean sub-STrad of ~ 2.7 °C were reconstructed for the Holocene and mIG-7 (Figure 4, Figure 5D), indicating similar-to-modern conditions. The relative abundances of the *Antarctissa* gp, a group ecologically associated with the APF, increased over each mIG (Figure 3G). Both sub-STrad and radiolarian assemblages suggest a northward migration of the front towards the MD11-3353 core site immediately after weaker pIGs. Mean SSTdiat of 5.5 °C and mean TEX_L^{86} SST of 6 °C in core MD11-3353 during the Holocene (Figure 4, Figure 5B-C) are above the APF SST range. In this case, TEX_L^{86} SST indicate slightly warmer-than-modern conditions, whereas SSTdiat agrees with sub-STrad, both recording similar-to-modern conditions. Thus, based on SSTdiat, sub-STrad and *Antarctissa* gp abundances in core MD11-3353, we propose that the APF may have shifted from the Fawn Trough to its modern position upstream of the KP very early in the Holocene and MIS 7.5. Additional SST and/or sub-ST data covering the late Holocene and/or the MIS 7.5 in cores from the Fawn Trough would be necessary to confirm that last statement. But if true, during

these two interglacials, the APF may have been sitting in the Fawn Trough for only a few thousands of years.

Again, downstream of the KP, the mean sub-STrad of 5.2 °C in core MD12-3396CQ during the Holocene is too high to track θ_{min} 2°C. However, it indicates slightly warmer-than-modern conditions and we therefore propose that the mean APF and SAF were located slightly south relative to their modern position (Figure 6C).

*** Figure 6 ***

5.3 Implications

The ~ 6 – 7° northward shifts in the mean APF position during the last four glacials in the KP region suggested by our results are consistent with the previously suggested 5 – 10° latitudinal migration of the ACC (Gersonde et al., 2003; Gersonde et al., 2005; Abelmann et al., 2015; Benz et al., 2016). During these cold periods, we propose that the APF migrations in the KP region were initiated by variations in SO climate and enhanced by the regional bathymetry, the latter causing the shifts to occur rapidly in a "single" large amplitude movement, as demonstrated in climate simulations (Graham et al., 2012).

In the modern SO, eddy kinetic energy (EKE) hotspots are generated by interactions between ACC fronts and large bathymetric features, such as the KP. The resulting mesoscale eddies sustain strong vertical mixing, thus allowing for the injection of nutrients from deeper waters into the surface layer of the ocean (Tamsitt et al., 2017; Rintoul et al., 2018; Uchida et al., 2020) where they sustain high phytoplankton productivity (Blain et al., 2007; Pollard et al., 2009). Here we showed that the APF was located north of the KP at around 45 °S during the last four glacial periods. Congruent northward migrations of the SAF (Gersonde et al., 2003; Crosta et al., 2005; Benz et al., 2016) and of the STF (Howard and Prell, 1992; Becquey and Gersonde, 2003; Gersonde et al., 2003; Bard and Rickaby, 2009) indicate that that the main ACC flow was less concentrated against the northern tip of the KP, more zonal and probably wider compared to today. Conversely, the less intense ACC branch, associated to the SACCF, was probably flowing over the KP (Figure 6A). Such an oceanographic configuration would imply a reduced eddy activity downstream of KI and a lesser interaction between the ACC and the regional bottom topography, with potential impact on the water column structure.

The 90 ppm drop in atmospheric CO_2 concentration during glacial periods is mainly attributed to SO processes, including the surface isolation of the AZ (Sigman et al., 2021; and references therein). Strong stratification of the water column in the AZ during the last glacial has been attributed to high volumes of seasonal meltwater from the large Winter Sea Ice (WSI) (François et al., 1997; Shin et al., 2003; Abelmann et al., 2015) and decreased wind-driven upwelling (Wyrwoll et al., 2000; Toggweiler et al., 2006; Kohfeld et al., 2013). Here, we propose that the reduced eddy activity over and downstream of KP as an additional process further increasing surface isolation during the last four glacials though several processes. First, the less intense eddy activity may have decreased diapycnal mixing between the UCDW and the upper layers. Second, the lesser interaction with bottom topography may have decreased the sea-floor induced mixing (Rintoul, 2018). Both processes would have reduced upward mixing of deep, CO_2–rich waters and therefore the degassing of CO_2 to the atmosphere (Gottschalk et al., 2020). Additionally, the reduced eddy activity generated by the northward migration of the ACC probably contributed to the lower phytoplankton productivity south of 50°S downstream of KP during the last glacial period (Bareille et al., 1998; Dézileau et al., 2003) by lowering macro-nutrient input to the AASW.

Conversely, the ~ 5° southward shifts in the mean APF position during pIGs forced the APF to pass through the Fawn Trough and to form an "S" shape downstream. The SAF was congruently forced against the northern tip of the KP, turning south downstream of the obstacle. As such, we propose that the SAF and APF had stronger interactions with bathymetry than during glacials, which caused instabilities in the main flow and enhanced the eddy field downstream of the KP. Higher EKE downstream of the KP coupled with less buoyant AASW, due to lower volumes of seasonal sea-ice meltwater as suggested by a more southern WSI limit (Esper and Gersonde, 2014; Abelmann et al., 2015; Nair et al., 2019; Chadwick et al., 2020; Ghadi et al., 2020), point to a better regional mixing of the water column during pIGs. Additionally, the reduction of the AZ due to the unusual spread of the PFZ over a large band covering as much as 10 – 11 ° of latitude probably decreased the residence time of water in AZ surface while reducing the region where diatom productivity dominates, both processes reducing CO_2 biological uptake (Sigman et al., 2021; and references therein). The steady increase in the opal flux and steady decrease in diatom-bound $\delta^{15}N$ in core MD11-3353 over the Holocene (Studer et al., 2018), further support a northward migration of the high productivity and high nutrient supply regimes from the Fawn Trough during the HCO to the core site during the Late Holocene. The overall impact of EKE

variations and ACC-bottom topography between glacials and interglacials on atmospheric CO_2 concentrations is however difficult to estimate, as the fronts' variability effect on the SO carbon sink is poorly represented in climate models (Chapman et al., 2020).

Over the last decades, a strong reduction in KI ice sheet has been observed and attributed to a ~ 1 °C increase of atmospheric and oceanic temperatures along with a southward migration of the wind circulation due to a positive Southern Annular Mode (SAM) that relocated the regional moisture supply south (Favier et al., 2016). Our results show that the APF, and probably westerly winds, were located south of their modern position during all pIGs of the last 360 kyrs, when the SO climate was warmer than present (Capron et al., 2014). As temperatures are projected to increase over the next decades (IPCC, 2013), regional atmospheric and oceanic conditions may progressively revert from mIG to pIG conditions. We propose that this may result in a permanent relocation of the APF at the Fawn Trough, constraining regional moisture to the south, which will cause further shrinking of KI glaciers. The eddy field intensity and, thus, mixing of the water column should increase east of KI due to the main ACC branch being gradually more constrained against the northern tip of the KP. Siliceous productivity may become restrained to latitudes south of the Fawn Trough. If this comes true, we expect a decrease in efficiency of the soft tissue pump east of the KI where, today, abrupt events of surface water subduction sink large amounts of particulate organic carbon to the ocean interior (Llort et al., 2017).

Conclusion

We generated two new, high-resolution temperature records of oceanic sub-ST and SST for the western part of the Kerguelen Plateau, covering the last 360 and 150 kyrs, respectively. These results, along with variations in relative abundances of radiolarian assemblages, allowed us to interpret hydrological fronts' mean position off KP during periods such as glacials, peak (pIGs) and mild-interglacials (mIGs), with modern oceanographic conditions as a reference. During the last four glacials, our results suggest that the APF shifted north of the KP. Under pIG conditions and warmer mIGs (MIS 5.5 and MIS 9.3), our results suggest that the APF shifted by ~ 5° to the south to sit in the Fawn Trough. During cooler mIGs (MIS 7.5 and Holocene), the oceanography was rather similar to the modern situation. The hydrological front migrations and the associated changes in the interaction of the ACC flow with the

bathymetric high possibly had important implications for water column structure over and east of the KP, leading to an increased stratification (mixing) during glacials (peak-interglacials). The northerly zonal ACC flow during glacial periods reduced such interaction and, consequently, eddy formation. We propose that the causal reduced vertical mixing participated to the observed Antarctic surface water stratification. Conversely during pIGs, the greater interaction of the ACC flow with the KP along with the "S" shaped flow over the KP increased eddy-forced mixing, thus homogenising the water column more efficiently. However, high-resolution models are necessary to better assess these oceanographic changes and their potential impacts on ocean stratification and regional productivity in a complex sector that is important for anthropogenic CO_2 uptake.

Acknowledgements

We are grateful to people from the MD185 and MD189 oceanographic expeditions operated by the IPEV-TAAF. Financial support to this study was provided by LEFE DYNACC and LEFE GLACOCEAN projects for the diatom part. Funding for this project was provided by the New Zealand Ministry of Business, Innovation and Employment through the Antarctic Science Platform (ANTA1801) and Global Change through Time Program (both to GC) along with the JSPS KAKENHI (Grants-in-Aid for Scientific Research) Grant Number JP17H06318 attributed to MI-TI for the radiolarian part and MCM salary. We are also thankful to IDEX Bordeaux Visiting Scholar scheme that funded GC stay at EPOC in 2017. We thank the team of the TANDETRON National French ^{14}C AMS facility, whom measured ^{14}C radiocarbon dates on core MD84-551. Finally, we are grateful to Dr. Helen Bostock and one anonymous reviewer for their constructive comments.

Authors' contribution

MCM produced the radiolarian census counts, sub-STrad and wrote the initial version of the manuscript. XC and GC designed the study. XC produced the diatom census counts and the SSTdiat. GC trained MCM in radiolarian taxonomy and made the radiolarian modern reference database available. EM and AM provided access to the cores. EM provided ^{14}C data and age model of core MD84-551 (supplementary material 4). OT produced microscopic

slides for diatom census counting. MI and TI provided supervision along with logistical and financial support to MCM's PhD. All authors interacted on the results, interpretations and successive versions of the manuscript.

Conflict of interest

The authors declare no conflict of interest.

References

Abelmann, A., Brathauer, U., Gersonde, R., Sieger, R., Zielinski, U., 1999. Radiolarian-based transfer function for the estimation of sea surface temperatures in the Southern Ocean (Atlantic sector). Paleoceanography 14, 410–421. https://doi.org/10.1029/1998PA900024

Abelmann, A., Gersonde, R., 1991. Biosiliceous flux in the Southern Ocean. Marine Chemistry 35, 503–536.

Abelmann, A., Gersonde, R., Cortese, G., Kuhn, G., Smetacek, V., 2006. Extensive phytoplankton blooms in the Atlantic sector of the glacial Southern Ocean. Paleoceanography 21. https://doi.org/10.1029/2005PA001199

Abelmann, A., Gersonde, R., Knorr, G., Zhang, X., Chapligin, B., Maier, E., Esper, O., Friedrichsen, H., Lohmann, G., Meyer, H., Tiedemann, R., 2015. The seasonal sea-ice zone in the glacial Southern Ocean as a carbon sink. Nature Communications 6. https://doi.org/10.1038/ncomms9136

Abelmann, A., Gowin, M.M., 1997. Spatial distribution pattern of living polycystine radiolarian taxa - baseline study for paleoenvironmental reconstructions in the Southern Ocean (Atlantic sector). Marine Micropaleontology 30, 3–28. https://doi.org/https://doi.org/10.1016/S0377-8398(96)00021-7

Abelmann, A., Nimmergut, A., 2005. Radiolarians in the Sea of Okhotsk and their ecological implication for paleoenvironmental reconstructions. Deep Sea Research Part II: Topical Studies in Oceanography 52, 2302–2331. https://doi.org/10.1016/j.dsr2.2005.07.009

Amante, C., Eakins, B.W., 2008. ETOPO1, 1 Arc-Minute Global Relief Model: Procedures, Data Sources and Analysis. NOAA Technical Memorandum NESDIS NGDC-24. National Geophysical Data Center, NOAA. https://doi.org/10.7289/V5C8276M

Anilkumar, N., Luis, A.J., Somayajulu, Y.K., Ramesh Babu, V., Dash, M.K., Pednekar, S.M., Babu, K.N., Sudhakar, M., Pandey, P.C., 2006. Fronts, water masses and heat content variability in the Western Indian sector of the Southern Ocean during austral summer 2004. Journal of Marine Systems 63, 20–34. https://doi.org/10.1016/j.jmarsys.2006.04.009

Bard, E., Rickaby, R.E.M., 2009. Migration of the subtropical front as a modulator of glacial climate. Nature 460, 380–383. https://doi.org/10.1038/nature08189

Bareille, G., Grousset, F.E., Labracherie, M., Labeyrie, L.D., Petit, J.-R., 1994. Origin of detrital fluxes in the southeast Indian Ocean during the last climatic cycles. Paleoceanography 9, 799–819. https://doi.org/https://doi.org/10.1029/94PA01946

Bareille, G., Labracherie, M., Bertrand, P., Labeyrie, L., Lavaux, G., Dignan, M., 1998. Glacial–interglacial changes in the accumulation rates of major biogenic components in Southern Indian Ocean sediments. Journal of Marine Systems 17, 527–539.

Bazin, L., Landais, A., Lemieux-Dudon, B., Toyé Mahamadou Kele, H., Veres, D., Parrenin, F., Martinerie, P., Ritz, C., Capron, E., Lipenkov, V., Loutre, M.-F., Raynaud, D., Vinther, B., Svensson, A., Rasmussen, S.O., Severi, M., Blunier, T., Leuenberger, M., Fischer, H., Masson-Delmotte, V., Chappellaz, J., Wolff, E., 2013. An optimized multi-proxy, multi-site Antarctic ice and gas orbital chronology (AICC2012): 120–800 ka. Climate of the Past 9, 1715–1731. https://doi.org/10.5194/cp-9-1715-2013

Bazin, L., Landais, A., Lemieux-Dudon, B., Toyé, M.K.H., Veres, D., Parrenin, F., Martinerie, P., et al., 2013. Chronology for Ice Core EDC. https://doi.org/10.1594/PANGAEA.824894

Becquey, S., Gersonde, R., 2003. A 0.55-Ma paleotemperature record from the Subantarctic zone: Implications for Antarctic Circumpolar Current development. Paleoceanography 18. https://doi.org/10.1029/2000PA000576

Belkin, I.M., 1989. Alteration of the front distributions in the Southern Ocean near the Crozet Plateau. DoM. Acad. Sci. USSR, Earth Sci. Sec., Engl. Transl. 308, 265–268.

Belkin, I.M., Gordon, A.L., 1996. Southern Ocean fronts from the Greenwich meridian to Tasmania. J. Geophys. Res. 101, 3675–3696. https://doi.org/10.1029/95JC027

Benz, V., Esper, O., Gersonde, R., Lamy, F., Tiedemann, R., 2016. Last Glacial Maximum sea surface temperature and sea-ice extent in the Pacific sector of the Southern Ocean. Quaternary Science Reviews 146, 216–237. https://doi.org/10.1016/j.quascirev.2016.06.006

Bianchi, C., Gersonde, R., 2004. Climate evolution at the last deglaciation: the role of the Southern Ocean. Earth and Planetary Science Letters 228, 407–424. https://doi.org/10.1016/j.epsl.2004.10.003

Blain, S., Quéguiner, B., Armand, L., Belviso, S., Bombled, B., Bopp, L., Bowie, A., Brunet, C., Brussaard, C., Carlotti, F., Christaki, U., Corbière, A., Durand, I., Ebersbach, F., Fuda, J.-L., Garcia, N., Gerringa, L., Griffiths, B., Guigue, C., Guillerm, C., Jacquet, S., Jeandel, C., Laan, P., Lefèvre, D., Lo Monaco, C., Malits, A., Mosseri, J., Obernosterer, I., Park, Y.-H., Picheral, M., Pondaven, P., Remenyi, T., Sandroni, V., Sarthou, G., Savoye, N., Scouarnec, L., Souhaut, M., Thuiller, D., Timmermans, K., Trull, T., Uitz, J., van Beek, P., Veldhuis, M., Vincent, D., Viollier, E., Vong, L., Wagener, T., 2007. Effect of natural iron fertilization on carbon sequestration in the Southern Ocean. Nature 446, 1070–1074. https://doi.org/10.1038/nature05700

Boex, J., Fogwill, C., Harrison, S., Glasser, N.F., Hein, A., Schnabel, C., Xu, S., 2013. Rapid thinning of the late Pleistocene Patagonian Ice Sheet followed migration of the Southern Westerlies. Scientific Reports 3. https://doi.org/10.1038/srep02118

Boltovskoy, D., 2017. Vertical distribution patterns of Radiolaria Polycystina (Protista) in the World Ocean: living ranges, isothermal submersion and settling shells. Journal of Plankton Research 39, 330–349. https://doi.org/10.1093/plankt/fbx003

Boltovskoy, D., 1998. Classification and distribution of South Atlantic recent polycystine Radiolaria. Palaeontologia Electronica 1, 116. https://doi.org/https://doi.org/10.26879/98006

Boltovskoy, D., Anderson, O.R., Correa, N.M., 2017. Radiolaria and Phaeodaria, in: Archibald, J.M., Simpson, A.G.B., Slamovits, C.H., Margulis, L., Melkonian, M., Chapman, D.J., Corliss, J.O. (Eds.), Handbook of the Protists. Springer International Publishing, Cham, pp. 1–33. https://doi.org/10.1007/978-3-319-32669-6_19-2

Bostock, H.C., Barrows, T.T., Carter, L., Chase, Z., Cortese, G., Dunbar, G.B., Ellwood, M., Hayward, B., Howard, W., Neil, H.L., Noble, T.L., Mackintosh, A., Moss, P.T., Moy, A.D., White, D., Williams, M.J.M., Armand, L.K., 2013. A review of the Australian–New Zealand sector of the Southern Ocean over the last 30 ka (Aus-INTIMATE project). Quaternary Science Reviews 74, 35–57. https://doi.org/10.1016/j.quascirev.2012.07.018

Botnikov, V. N., 1963. Geographic position of the Antarctic Convergence Zone in the Southern Ocean (in Russian), Sov. Antarct. Exped. Inf. Bull., 41, 19–24 (Sov. Antarct. Exped. Inf. Bull., Engl. Transl., 4, 324–327, 1963.)

Bronk Ramsey, C., 2009. Dealing with outliers and offsets in radiocarbon dating. Radiocarbon, 51(3), 1023–1045.

Chadwick, M., Allen, C.S., Sime, L.C., Hillenbrand, C.-D., 2020. Analysing the timing of peak warming and minimum winter sea-ice extent in the Southern Ocean during MIS 5e. Quaternary Science Reviews 229, 106134. https://doi.org/10.1016/j.quascirev.2019.106134

Chapman, C.C., 2014. Southern Ocean jets and how to find them: Improving and comparing common jet detection methods. J. Geophys. Res. Oceans 119, 4318–4339. https://doi.org/10.1002/2014JC009810

Chapman, C.C., 2017. New Perspectives on Frontal Variability in the Southern Ocean. Journal of Physical Oceanography 47, 1151–1168. https://doi.org/10.1175/JPO-D-16-0222.1

Chapman, C.C., Lea, M.-A., Meyer, A., Sallée, J.-B., Hindell, M., 2020. Defining Southern Ocean fronts and their influence on biological and physical processes in a changing climate. Nature Climate Change 10, 209–219. https://doi.org/10.1038/s41558-020-0705-4

Civel-Mazens, M., Crosta, X., Cortese, G., Michel, E., Mazaud, A., Ther, O., Ikehara, M., Itaki, T., 2021. Impact of the Agulhas Return Current on the oceanography of the Kerguelen Plateau region, Southern Ocean, over the last 40 kyrs. Quaternary Science Reviews 251. https://doi.org/10.1016/j.quascirev.2020.106711

Cortese, G., Abelmann, A., 2002. Radiolarian-based paleotemperatures during the last 160 kyr at ODP Site 1089 (Southern Ocean, Atlantic Sector). Palaeogeography, Palaeoclimatology, Palaeoecology 182, 259–286.

Cortese, G., Abelmann, A., Gersonde, R., 2007. The last five glacial-interglacial transitions: A high-resolution 450,000-year record from the subantarctic Atlantic. Paleoceanography 22. https://doi.org/10.1029/2007PA001457

Crosta, X., Beucher, C., Pahnke, K., Brzezinski, M.A., 2007. Silicic acid leakage from the Southern Ocean: Opposing effects of nutrient uptake and oceanic circulation. Geophysical Research Letters 34. https://doi.org/10.1029/2006GL029083

Crosta, X., Shemesh, A., Etourneau, J., Yam, R., Billy, I., Pichon, J.J., 2005. Nutrient cycling in the Indian sector of the Southern Ocean over the last 50,000 years. Global Biogeochemical Cycles 19. https://doi.org/10.1029/2004GB002344

Crosta, X., Shukla, S.K., Ther, O., Ikehara, M., Yamane, M., Yokoyama, Y., 2020. Last Abundant Appearance Datum of Hemidiscus karstenii driven by climate change. Marine Micropaleontology 157. https://doi.org/10.1016/j.marmicro.2020.101861

Crosta, X., Sturm, A., Armand, L., Pichon, J.-J., 2004. Late Quaternary sea ice history in the Indian sector of the Southern Ocean as recorded by diatom assemblages. Marine Micropaleontology 50, 209–223. https://doi.org/10.1016/S0377-8398(03)00072-0

Dezileau, L., Reyss, J.L., Lemoine, F., 2003. Late Quaternary changes in biogenic opal fluxes in the Southern Indian Ocean. Marine Geology 202, 143–158. https://doi.org/10.1016/S0025-3227(03)00283-4

DiTullio, G.R., Geesey, M.E., Jones, D.R., Daly, K.L., Campbell, L., Smith Jr, W.O., 2003. Phytoplankton assemblage structure and primary productivity along 170 W in the South Pacific Ocean. Marine Ecology Progress Series 255, 55–80.

Dong, S., Sprintall, J., Gille, S.T., 2006. Location of the Antarctic polar front from AMSR-E satellite sea surface temperature measurements. Journal of Physical Oceanography 36, 2075–2089.

Dumont, M., Pichevin, L., Geibert, W., Crosta, X., Michel, E., Moreton, S., Dobby, K., Ganeshram, R., 2020. The nature of deep overturning and reconfigurations of the silicon cycle across the last deglaciation. Nature Communications 11. https://doi.org/10.1038/s41467-020-15101-6

Esper, O., Gersonde, R., 2014. Quaternary surface water temperature estimations: New diatom transfer functions for the Southern Ocean. Palaeogeography, Palaeoclimatology, Palaeoecology 414, 1–19. https://doi.org/10.1016/j.palaeo.2014.08.008

Favier, V., Verfaillie, D., Berhier, E., Menegoz, M., Jomelli, V., Kay, J.E., Ducret, L., Malbéteau, Y., Brunstein, D., Gallée, H., Park, Y.-H., Rinterknecht, V., 2016. Atmospheric drying as the main driver of dramatic glacier wastage in the southern Indian Ocean. Scientific Reports 6. https://doi.org/10.1038/srep32396

Firing, Y.L., Chereskin, T.K., Mazloff, M.R., 2011. Vertical structure and transport of the Antarctic Circumpolar Current in Drake Passage from direct velocity observations. Journal of Geophysical Research 116. https://doi.org/10.1029/2011JC006999

Francois, R., Altabet, M.A., Yu, E.-F., Sigman, D.M., Bacon, M.P., Frank, M., Bohrmann, G., Bareille, G., Labeyrie, L.D., 1997. Contribution of Southern Ocean surface-water stratification to low atmospheric CO2 concentrations during the last glacial period. Nature 389, 929–935.

Freeman, N.M., Lovenduski, N.S., 2016. Mapping the Antarctic Polar Front: weekly realizations from 2002 to 2014. Earth System Science Data 8, 191–198. https://doi.org/10.5194/essd-8-191-2016

Freeman, N.M., Lovenduski, N.S., Gent, P.R., 2016. Temporal variability in the Antarctic Polar Front (2002-2014). Journal of Geophysical Research: Oceans 121, 7263–7276. https://doi.org/10.1002/2016JC012145

Galbraith, E.D., Jaccard, S.L., 2015. Deglacial weakening of the oceanic soft tissue pump: global constraints from sedimentary nitrogen isotopes and oxygenation proxies. Quaternary Science Reviews 109, 38–48. https://doi.org/10.1016/j.quascirev.2014.11.012

Gersonde, R., Abelmann, A., Brathauer, U., Becquey, S., Bianchi, C., Cortese, G., Grobe, H., Kuhn, G., Niebler, H.-S., Segl, M., Sieger, R., Zielinski, U., Fütterer, D.K., 2003. Last glacial sea surface temperatures and sea-ice extent in the Southern Ocean (Atlantic-Indian sector): A multiproxy approach. Paleoceanography 18. https://doi.org/10.1029/2002PA000809

Gersonde, R., Crosta, X., Abelmann, A., Armand, L., 2005. Sea-surface temperature and sea ice distribution of the Southern Ocean at the EPILOG Last Glacial Maximum—a circum-Antarctic view based on siliceous microfossil records. Quaternary Science Reviews 24, 869–896. https://doi.org/10.1016/j.quascirev.2004.07.015

Ghadi, P., Nair, A., Crosta, X., Mohan, R., Manoj, M.C., Meloth, T., 2020. Antarctic sea-ice and palaeoproductivity variation over the last 156,000 years in the Indian sector of Southern Ocean. Marine Micropaleontology 160. https://doi.org/10.1016/j.marmicro.2020.101894

Gottschalk, J., Michel, E., Thöle, L.M., Studer, A.S., Hasenfratz, A.P., Schmid, N., Butzin, M., Mazaud, A., Martínez García, A., Szidat, S., Jaccard, S.L., 2020. Glacial heterogeneity in Southern Ocean carbon storage abated by fast South Indian deglacial carbon release. Nature Communications 11. https://doi.org/10.1038/s41467-020-20034-1

Govin, A., Capron, E., Tzedakis, P.C., Verheyden, S., Ghaleb, B., Hillaire-Marcel, C., St-Onge, G., Stoner, J.S., Bassinot, F., Bazin, L., 2015. Sequence of events from the onset to the demise of the Last Interglacial: Evaluating strengths and limitations of chronologies used in climatic archives. Quaternary Science Reviews 129, 1–36. https://doi.org/10.1016/j.quascirev.2015.09.018

Graham, R.M., De Boer, A.M., Heywood, K.J., Chapman, M.R., Stevens, D.P., 2012. Southern Ocean fronts: controlled by wind or topography? Journal of Geophysical Research: Oceans 117. https://doi.org/10.1029/2012JC007887

Graham, R.M., De Boer, A.M., Van Sebille, E., Kohfeld, K.E., Schlosser, C., 2015. Inferring source regions and supply mechanisms of iron in the Southern Ocean from satellite chlorophyll data. Deep Sea Research Part I: Oceanographic Research Papers 104, 9–25. https://doi.org/10.1016/j.dsr.2015.05.007

Guiot, J., de Vernal, A., 2011. Is spatial autocorrelation introducing biases in the apparent accuracy of paleoclimatic reconstructions? Quaternary Science Reviews 30, 1965–1972. https://doi.org/10.1016/j.quascirev.2011.04.022

Hammer, O. Harper, D., A., T., Ryan, P., D., 2001. PAST: Paleontological statistics software package for education and data analysis. Palaeontologia Electronica 4(1): 9pp.

Hays, J.D., Imbrie, J., Shackelton, N.J., 1976. Variations in the Earth's Orbit: Pacemaker of the Ice Ages. Science 194, 1121–1132.

Hays, J.D., Morley, J.J., 2003. The Sea of Okhotsk: A Window on the Ice Age Ocean. Deep Sea Research Part I: Oceanographic Research Papers 50, 1481–1506. https://doi.org/10.1016/j.dsr.2003.08.002

Hernández-Almeida, I., Boltovskoy, D., Kruglikova, S.B., Cortese, G., 2020. A new radiolarian transfer function for the Pacific Ocean and application to fossil records: Assessing potential and limitations for the last glacial-interglacial cycle. Global and Planetary Change 190. https://doi.org/10.1016/j.gloplacha.2020.103186

Hogg, A., Hua, Q., Blackwell, P., Niu, M., Buck, C., Guilderson, T., Zimmerman, S. 2013. SHCal13 Southern Hemisphere Calibration, 0–50,000 Years cal BP. Radiocarbon, 55(4), 1889-1903. https://doi:10.2458/azu_js_rc.55.16783

Howard, W.R., Prell, W. L., 1992. Late Quaternary surface circulation of the Southern Indian Ocean and its relations to orbital variations. Paleoceanography 7, 79–117. https://doi.org/https://doi.org/10.1029/91PA02994

Hughes, C.W., 2005. Nonlinear vorticity balance of the Antarctic Circumpolar Current. Journal of Geophysical Research 110. https://doi.org/10.1029/2004JC002753

Hughes, C.W., Ash, E.R., 2001. Eddy forcing of the mean flow in the Southern Ocean. Journal of Geophysical Research 106, 2713–2722.

Imbrie, J., Kipp, N.G., 1971. A new micropaleontological method for paleoclimatology: application to a Late Pleistocene Caribbean core. The Late Cenozoic Glacial Ages.

IPCC, 2013. Climate Change 2013: The Physical Science Basis. Contribution of Working Group I to the Fifth Assessment Report of the Intergovernmental Panel on Climate Change [Stocker, T.F., D. Qin, G.-K. Plattner, M. Tignor, S.K. Allen, J. Boschung, A. Nauels, Y. Xia, V. Bex and P.M. Midgley (eds.)]. Cambridge University Press, Cambridge, United Kingdom and New York, NY, USA, 1535 pp. https://doi:10.1017/CBO9781107415324.

Itaki, T., Sagawa, T., Kubota, Y., 2018. Data report: pleistocene radiolarian biostratigraphy, IODP expedition 346 site U1427. In: Tada, R., Murray, R.W., Alvarez Zarikian, C.A. (Eds.), Expedition 346 Scientists, Proceedings of the Integrated Ocean Drilling Program, vol. 346. Integrated Ocean Drilling Program), College Station, TX. https://doi.org/10.2204/iodp.proc.346.202.2018.

Itaki, T., Uchida, M., Kim, S., Shin, H.-S., Tada, R., Khim, B.-K., 2009. Late Pleistocene stratigraphy and palaeoceanographic implications in northern Bering Sea slope sediments: evidence from the radiolarian species Cycladophora davisiana. Journal of Quaternary Science 24, 856–865. https://doi.org/10.1002/jqs.1356

Jaccard, S.L., Galbraith, E.D., Martínez-García, A., Anderson, R.F., 2016. Covariation of deep Southern Ocean oxygenation and atmospheric CO2 through the last ice age. Nature 530, 207–210. https://doi.org/10.1038/nature16514

Jouzel, J., Masson-Delmotte, V., Cattani, O., Dreyfus, G., Falourd, S., Hoffmann, G., Minster, B., Nouet, J., Barnola, J.M., Chappellaz, J., Fischer, H., Gallet, J.C., Johnsen, S., Leuenberger, M., Loulergue, L., Luethi, D., Oerter, H., Parrenin, F., Raisbeck, G., Raynaud, D., Schilt, A., Schwander, J., Selmo, E., Souchez, R., Spahni, R., Stauffer, B., Steffensen, J.P., Stenni, B., Stocker, T.F., Tison, J.L., Werner, M., Wolff, E.W., 2007. Orbital and Millennial Antarctic Climate Variability over the Past 800,000 Years. Science 317, 793–796. https://doi.org/10.1126/science.1141038

Katsuki, K., Ikehara, M., Yokoyama, Y., Yamane, M., Khim, B.-K., 2012. Holocene migration of oceanic front systems over the Conrad Rise in the Indian Sector of the Southern Ocean. Journal of Quaternary Science 27, 203–210. https://doi.org/10.1002/jqs.1535

Kim, J.-H., Crosta, X., Michel, E., Schouten, S., Duprat, J., Sinninghe Damsté, J.S., 2009. Impact of lateral transport on organic proxies in the Southern Ocean. Quaternary Research 71, 246–250. https://doi.org/10.1016/j.yqres.2008.10.005

Klocker, A., 2018. Opening the window to the Southern Ocean: The role of jet dynamics. Science Advances 4. https://doi.org/10.1126/sciadv.aao4719

Kohfeld, K.E., Graham, R.M., de Boer, A.M., Sime, L.C., Wolff, E.W., Le Quéré, C., Bopp, L., 2013. Southern Hemisphere westerly wind changes during the Last Glacial Maximum: paleo-data synthesis. Quaternary Science Reviews 68, 76–95. https://doi.org/10.1016/j.quascirev.2013.01.017

Labracherie, M., Labeyrie, L.D., Duprat, J., Bard, E., Arnold, M., Pichon, J.-J., Duplessy, J.-C., 1989. The Last Deglaciation in the Southern Ocean. Paleoceanography 4, 629–638. https://doi.org/10.1029/PA004i006p00629

Langlais, C.E., Lenton, A., Matear, R., Monselesan, D., Legresy, B., Cougnon, E., Rintoul, S., 2017. Stationary Rossby waves dominate subduction of anthropogenic carbon in the Southern Ocean. Scientific Reports 7. https://doi.org/10.1038/s41598-017-17292-3

Lawler, K.A., Cortese, G., Civel-Mazens, M., Bostock, H., Crosta, X., Leventer, A., Lowe, V., Rogers, J., Armand, L.K., submitted. Southern Ocean RAdiolarian Dataset (SO-RAD): a new compilation of modern radiolarian census data. Earth System Science Data. *The associated dataset is under review:* https://doi.pangaea.de/10.1594/PANGAEA.929903

Llort, J., Langlais, C., Matear, R., Moreau, S., Lenton, A., Strutton, P.G., 2018. Evaluating Southern Ocean Carbon Eddy-Pump From Biogeochemical-Argo Floats. Journal of Geophysical Research: Oceans 123, 971–984. https://doi.org/10.1002/2017JC012861

Locarnini, R.A., Mishonov, A.V., Antonov, J.I., Boyer, T.P., Garcia, H.E., Baranova, O.K., Zweng, M.M., Paver, C.R., Reagan, J.R., Johnson, D.R., Hamilton, M., Seidov, D., 2013. In: Levitus, S., Mishonov, A., Technical (Eds.), World Ocean Atlas 2013, Volume 1: Temperature, NOAA Atlas NESDIS, vol. 73, p. 40.

Locarnini, R.A., Mishonov, A.V., Baranova, O.K., Boyer, T.P., Zweng, M.M., Garcia, H.E., Reagan, J.R., Seidov, D., Weathers, K.W., Paver, C. R., Smolyar, I.V., 2019. World Ocean Atlas 2018, Volume 1: Temperature. A. Mishonov Technical Editor, NOAA Atlas NESDIS vol. 81.

Lüer, V., Cortese, G., Neil, H.L., Hollis, C.J., Willems, H., 2009. Radiolarian-based sea surface temperatures and paleoceanographic changes during the Late Pleistocene–Holocene in the subantarctic southwest Pacific. Marine Micropaleontology 70, 151–165. https://doi.org/10.1016/j.marmicro.2008.12.002

Luis, A.J., Sudhakar, M., 2009. Upper-ocean hydrodynamics along meridional sections in the southwest Indian sector of the Southern Ocean during austral summer 2007. Polar Science 3, 13–30. https://doi.org/10.1016/j.polar.2009.03.001

Lutjeharms, J.E., Valentine, H.R., 1984. Southern Ocean thermal fronts south of Africa. Deep Sea Research Part A. Oceanographic Research Papers 31, 1461–1475.

Marshall, J., Speer, K., 2012. Closure of the meridional overturning circulation through Southern Ocean upwelling. Nature Geoscience 5, 171–180. https://doi.org/10.1038/ngeo1391

Matsumoto, K., Chase, Z., Kohfeld, K., 2014. Different mechanisms of silicic acid leakage and their biogeochemical consequences. Paleoceanography 29, 252–254.

https://doi.org/10.1002/2013PA002588

Matsumoto, K., Sarmiento, J.L., 2008. A corollary to the silicic acid leakage hypothesis. Paleoceanography 23. https://doi.org/10.1029/2007PA001515

Matsumoto, K., Sarmiento, J.L., Brzezinski, M.A., 2002. Silicic acid leakage from the Southern Ocean: A possible explanation for glacial atmospheric pCO_2. Global Biogeochemical Cycles 16, 5-1-5–23. https://doi.org/10.1029/2001GB001442

Matsuzaki, K.M., Itaki, T., 2017. New northwest Pacific radiolarian data as a tool to estimate past sea surface and intermediate water temperatures. Paleoceanography 32, 218–245. https://doi.org/10.1002/2017PA003057

Matsuzaki, K.M., Itaki, T., Tada, R., 2019. Paleoceanographic changes in the Northern East China Sea during the last 400 kyr as inferred from radiolarian assemblages (IODP Site U1429). Progress in Earth and Planetary Science 6, 22. https://doi.org/10.1186/s40645-019-0256-3

Matul, A., Mohan, R., 2017. Distribution of Polycystine Radiolarians in Bottom Surface Sediments and Its Relation to Summer Sea Temperature in the High-Latitude North Atlantic. Frontiers in Marine Science 4, 330. https://doi.org/10.3389/fmars.2017.00330

Mazaud, A., Michel, E., 2011. MD185 Indien Sud-1 Cruise Report. RV Marion

Dufresne. https://doi.org/10.17600/11200030.

Mazaud, A., Michel, E., Dewilde, F., Turon, J.L., 2010. Variations of the Antarctic Circumpolar Current intensity during the past 500 ka. Geochemistry, Geophysics, Geosystems 11. https://doi.org/10.1029/2010GC003033

Mazaud, A., Sicre, M.A., Ezat, U., Pichon, J.J., Duprat, J., Laj, C., Kissel, C., Beaufort, L., Michel, E., Turon, J.L., 2002. Geomagnetic-assisted stratigraphy and sea surface temperature changes in core MD94-103 (Southern Indian Ocean): possible implications for North–South climatic relationships around H4. Earth and Planetary Science Letters 201, 159–170.

Mazloff, M.R., Heimbach, P., Wunsch, C., 2010. An Eddy-Permitting Southern Ocean State Estimate. Journal of Physical Oceanography 40, 880–899. https://doi.org/10.1175/2009JPO4236.1

Moore, J.K., Abbott, M.R., Richman, J.G., 1999. Location and dynamics of the Antarctic Polar Front from satellite sea surface temperature data. Journal of Geophysical Research: Oceans 104, 3059–3073.

Morley, J. J., Hays, J. D., (1983): Oceanographic conditions associated with high abundances of the radiolarian Cycladophora davisiana. Earth Planet. Sci. Lett., 66, pp. 63–72.

Nair, A., Mohan, R., Crosta, X., Manoj, M.C., Thamban, M., Marieu, V., 2019. Southern Ocean sea ice and frontal changes during the Late Quaternary and their linkages to Asian summer monsoon. Quaternary Science Reviews 213, 93–104. https://doi.org/10.1016/j.quascirev.2019.04.007

Nair, A., Mohan, R., Manoj, M.C., Thamban, M., 2015. Glacial-interglacial variability in diatom abundance and valve size: Implications for Southern Ocean paleoceanography. Paleoceanography 30, 1245–1260. https://doi.org/10.1002/2014PA002680

Niiler, P.P., Maximenko, N.A., McWilliams, J.C., 2003. Dynamically balanced absolute sea level of the global ocean derived from near-surface velocity observations. Geophysical Research Letters 30. https://doi.org/10.1029/2003GL018628

Orme, L.C., Crosta, X., Miettinen, A., Divine, D.V., Husum, K., Isaksson, E., Wacker, L., Mohan, R., Ther, O., Ikehara, M., 2020. Sea surface temperature in the Indian sector of the Southern Ocean over the Late Glacial and Holocene. Climate of the Past 16, 1451–1467. https://doi.org/10.5194/cp-16-1451-2020

Orsi, A.H., Whitworth, T., 2005. Hydrographic Atlas of the World Ocean Circulation Experiment (WOCE) Volume 1: Southern Ocean. Retrieved from https://escholarship.org/uc/item/3xh7d30p

Orsi, A.H., Whitworth III, T., Nowlin Jr, W.D., 1995. On the meridional extent and fronts of the Antarctic Circumpolar Current. Deep Sea Research Part I: Oceanographic Research Papers 42, 641–673.

Pahnke, K., Goldstein, S.L., Hemming, S.R., 2008. Abrupt changes in Antarctic Intermediate Water circulation over the past 25,000 years. Nature Geoscience 1, 870–874. https://doi.org/10.1038/ngeo360

Pahnke, K., Zahn, R., 2005. Southern Hemisphere water mass conversion linked with North Atlantic climate variability. Science 307, 1741–1746.

Palter, J.B., Marinov, I., Sarmiento, J.L., Gruber, N., 2013. Large-Scale, Persistent Nutrient Fronts of the World Ocean: Impacts on Biogeochemistry. Springer Berlin Heidelberg, Berlin, Heidelberg. https://doi.org/10.1007/698_2013_241

Panitz, S., Cortese, G., Neil, H.L., Diekmann, B., 2015. A radiolarian-based palaeoclimate history of Core Y9 (Northeast of Campbell Plateau, New Zealand) for the last 160 kyr. Marine Micropaleontology 116, 1–14. https://doi.org/10.1016/j.marmicro.2014.12.003

Park, Y.-H., Durand, I., Kestenare, E., Rougier, G., Zhou, M., d'Ovidio, F., Cotté, C., Lee, J.-H., 2014. Polar Front around the Kerguelen Islands: An up-to-date determination and associated circulation of surface/subsurface waters. Journal of Geophysical Research: Oceans 119, 6575–6592. https://doi.org/10.1002/2014JC010061

Park, Y.-H., Gamberoni, L., Charriaud, E., 1993. Frontal structure, water masses, and circulation in the Crozet Basin. Journal of Geophysical Research: Oceans 98, 12361–12385.

Park, Y.-H., Roquet, F., Durand, I., Fuda, J.-L., 2008. Large-scale circulation over and around the Northern Kerguelen Plateau. Deep Sea Research Part II: Topical Studies in Oceanography 55, 566–581. https://doi.org/10.1016/j.dsr2.2007.12.030

Park, Y.-H., Park, T., Kim, T.-W., Lee, S.-H., Hong, C.-S., Lee, J.-H., Rio, M.-H., Pujol, M.-I., Ballarotta, M., Durand, I., Provost, C., 2019. Observations of the Antarctic Circumpolar Current Over the Udintsev Fracture Zone, the Narrowest Choke Point in the Southern Ocean. Journal of Geophysical Research: Oceans 124, 4511–4528. https://doi.org/10.1029/2019JC015024

Park, Y.-H., Vivier, F., Roquet, F., Kestenare, E., 2009. Direct observations of the ACC transport across the Kerguelen Plateau. Geophysical Research Letters 36. https://doi.org/10.1029/2009GL039617

Pauthenet, E., Roquet, F., Madec, G., Guinet, C., Hindell, M., McMahon, C.R., Harcourt, R., Nerini, D., 2018. Seasonal Meandering of the Polar Front Upstream of the Kerguelen Plateau. Geophysical Research Letters 45, 9774–9781. https://doi.org/10.1029/2018GL079614

Pichon, J.J., Labeyrie, L.D., Bareille, G., Labracherie, M., Duprat, J., Jouzel, J., 1992. Surface water temperature changes in the high latitudes of the Southern Hemisphere over the last Glacial-Interglacial cycle. Paleoceanography 7, 289–318. https://doi.org/10.1029/92PA00709

Pollard, R.T., Salter, I., Sanders, R.J., Lucas, M.I., Moore, C.M., Mills, R.A., Statham, P.J., Allen, J.T., Baker, A.R., Bakker, D.C.E., Charette, M.A., Fielding, S., Fones, G.R., French, M., Hickman, A.E., Holland, R.J., Hughes, J.A., Jickells, T.D., Lampitt, R.S., Morris, P.J., Nédélec, F.H., Nielsdóttir, M., Planquette, H., Popova, E.E., Poulton, A.J., Read, J.F., Seeyave, S., Smith, T., Stinchcombe, M., Taylor, S., Thomalla, S., Venables, H.J., Williamson, R., Zubkov, M.V., 2009. Southern Ocean deep-water carbon export enhanced by natural iron fertilization. Nature 457, 577–580. https://doi.org/10.1038/nature07716

Prell, W.L., 1985. The stability of low latitude sea surface temperatures: an evaluation of the CLIMAP reconstruction with emphasis on the positive SST anomalies. In: Rep. TR, vol. 25. U.S. Dep. of Energy, Washington, D.C, pp. 1-60

Ragueneau, O., Tréguer, P., Leynaert, A., Anderson, R.F., Brzezinski, M.A., DeMaster, D.J., Dugdale, R.C., Dymond, J., Fischer, G., François, R., 2000. A review of the Si cycle in the modern ocean: recent progress and missing gaps in the application of biogenic opal as a paleoproductivity proxy. Global and Planetary Change 26, 317–365.

Reimer P.J., Bard E., Bayliss A., et al., 2013. IntCal13 and Marine13 radiocarbon age calibration curves 0–50,000 years cal BP. Radiocarbon 55, 1869–1887.

Rigual-Hernández, A.S., Trull, T.W., Nodder, S.D., Flores, J.A., Bostock, H., Abrantes, F., Eriksen, R.S., Sierro, F.J., Davies, D.M., Ballegeer, A.-M., Fuertes, M.A., Northcote, L.C., 2020. Coccolithophore biodiversity controls carbonate export in the Southern Ocean. Biogeosciences 17, 245–263. https://doi.org/10.5194/bg-17-245-2020

Rigual-Hernández, A.S., Trull, T.W., Bray, S.G., Cortina, A., Armand, L.K., 2015. Latitudinal and temporal distributions of diatom populations in the pelagic waters of the Subantarctic and Polar Frontal zones of the Southern Ocean and their role in the biological pump. Biogeosciences 12, 5309–5337. https://doi.org/10.5194/bg-12-5309-2015

Rintoul, S.R., Naveira Garabato, A.C., 2013. Dynamics of the Southern Ocean Circulation, in: International Geophysics. Elsevier, pp. 471–492. https://doi.org/10.1016/B978-0-12-391851-2.00018-0

Rintoul, S.R., W. Hughes, C., Olbers, D., 2001. Chapter 4.6 The Antarctic circumpolar current system. International Geophysics. https://doi.org/10.1016/S0074-6142(01)80124-8

Rintoul, S.R., 2018. The global influence of localized dynamics in the Southern Ocean. Nature 558, 209–218. https://doi.org/10.1038/s41586-018-0182-3

Ronge, T.A., Steph, S., Tiedemann, R., Prange, M., Merkel, U., Nürnberg, D., Kuhn, G., 2015. Pushing the boundaries: Glacial/interglacial variability of intermediate and deep waters in the southwest Pacific over the last 350,000 years. Paleoceanography 30, 23–38. https://doi.org/10.1002/2014PA002727

Roquet, F., Park, Y.-H., Guinet, C., Bailleul, F., Charrassin, J. B., 2009. Observations of the Fawn Trough Current over the Kerguelen Plateau from instrumented elephant seals. Journal of Marine Systems 78, 377–393. https://doi.org/10.1016/j.jmarsys.2008.11.017

Sarmiento, J.L., Gruber, N., Brzezinski, M.A., Dunne, J.P., 2004. High-latitude controls of thermocline nutrients and low latitude biological productivity. Nature 427, 56–60. https://doi.org/doi:10.1038/nature10605

Schlitzer, R., 2000. Electronic Atlas of WOCE Hydrographic and Tracer Data Now Available, Eos Trans. AGU, 81(5), 45. https://www.ewoce.org/data/index.html (whp Bottle Data was used).

Schlitzer, R., 2002. Interactive analysis and visualization of geoscience data with Ocean Data View. Comput. Geosci. 28, 1211–1218. https://doi.org/10.1016/S0098-3004(02)00040-7

Shetye, S.S., Mohan, R., Nair, A., 2014. Latitudinal shifts in the Polar Front in Indian sector of the Southern Ocean: evidences from silicoflagellate assemblage. Geosciences Journal 18, 241–246. https://doi.org/10.1007/s12303-013-0061-8

Shin, S.-I., Liu, Z., Otto-Bliesner, B.L., Kutzbach, J.E., Vavrus, S.J., 2003. Southern Ocean sea-ice control of the glacial North Atlantic thermohaline circulation. Geophysical Research Letters 30. https://doi.org/10.1029/2002GL015513

Shukla, S.K., Crosta, X., Cortese, G., Nayak, G.N., 2013. Climate mediated size variability of diatom Fragilariopsis kerguelensis in the Southern Ocean. Quaternary Science Reviews 69, 49–58. https://doi.org/10.1016/j.quascirev.2013.03.005

Sigman, D.M., Fripiat, F., Studer, A.S., Kemeny, P.C., Martínez-García, A., Hain, M.P., Ai, X., Wang, X., Ren, H., Haug, G.H., 2021. The Southern Ocean during the ice ages: A review of the Antarctic surface isolation hypothesis, with comparison to the North Pacific. Quaternary Science Reviews 254, 106732. https://doi.org/10.1016/j.quascirev.2020.106732

Sokolov, S., Rintoul, S.R., 2002. Structure of Southern Ocean fronts at 140 E. Journal of Marine Systems 37, 151–184.

Sokolov, S., Rintoul, S.R., 2007. On the relationship between fronts of the Antarctic Circumpolar Current and surface chlorophyll concentrations in the Southern Ocean. Journal of Geophysical Research 112. https://doi.org/10.1029/2006JC004072

Sokolov, S., Rintoul, S.R., 2009a. Circumpolar structure and distribution of the Antarctic Circumpolar Current fronts: 1. Mean circumpolar paths. Journal of Geophysical Research 114. https://doi.org/10.1029/2008JC005108

Sokolov, S., Rintoul, S.R., 2009b. Circumpolar structure and distribution of the Antarctic Circumpolar Current fronts: 2. Variability and relationship to sea surface height. Journal of Geophysical Research 114. https://doi.org/10.1029/2008JC005248

Studer, A.S., Sigman, D.M., Martínez-García, A., Thöle, L.M., Michel, E., Jaccard, S.L., Lippold, J.A., Mazaud, A., Wang, X.T., Robinson, L.F., Adkins, J.F., Haug, G.H., 2018. Increased nutrient supply to the Southern Ocean during the Holocene and its implications for the pre-industrial atmospheric CO2 rise. Nature Geoscience 11, 756–760. https://doi.org/10.1038/s41561-018-0191-3

Stuiver, M., Reimer, P.,J., 1993. Extended 14C database and revised CALIB 3.0 14C age calibration program. Radiocarbon. 35, pp. 215–230.

Suzuki, N., Not, F., 2015. Biology and Ecology of Radiolaria. In: Ohtsuka S., Suzaki T., Horiguchi T., Suzuki N., Not F. (eds) Marine Protists. Springer, Tokyo. https://doi.org/10.1007/978-4-431-55130-0_8

Tamsitt, V., Drake, H.F., Morrison, A.K., Talley, L.D., Dufour, C.O., Gray, A.R., Griffies, S.M., Mazloff, M.R., Sarmiento, J.L., Wang, J., Weijer, W., 2017. Spiraling pathways of global deep waters to the surface of the Southern Ocean. Nature Communications 8. https://doi.org/10.1038/s41467-017-00197-0

Therón, R., Paillard, D., Cortijo, E., Flores, J.A., Vaquero, M., Sierro, F.J., Waelbroeck, C., 2003. Paleoanalogs: A multiplatform tool for reconstructing past environmental features. Geophysical Research Abstracts, Vol. 5, 05378.

Thöle, L.M., Amsler, H.E., Moretti, S., Auderset, A., Gilgannon, J., Lippold, J., Vogel, H., Crosta, X., Mazaud, A., Michel, E., Martínez-García, A., Jaccard, S.L., 2019. Glacial-interglacial dust and export production records from the Southern Indian Ocean. Earth and Planetary Science Letters 525, 115716. https://doi.org/10.1016/j.epsl.2019.115716

Toggweiler, J.R., Russell, J.L., Carson, S.R., 2006. Midlatitude westerlies, atmospheric CO_2, and climate change during the ice ages. Paleoceanography 21. https://doi.org/10.1029/2005PA001154

Tréguer, P.J., De La Rocha, C.L., 2013. The World Ocean Silica Cycle. Annual Review of Marine Science 5, 477–501. https://doi.org/10.1146/annurev-marine-121211-172346

Uchida, T., Balwada, D., P. Abernathey, R., A. McKinley, G., K. Smith, S., Lévy, M., 2020. Vertical eddy iron fluxes support primary production in the open Southern Ocean. Nature Communications 11. https://doi.org/10.1038/s41467-020-14955-0

Wessel, P., Luis, J.F., Uieda, L., Scharroo, R., Wobbe, F., Smith, W.H.F., Tian, D., 2019. The generic mapping tools version 6. G-cubed 20, 5556e5564. https://doi.org/10.1029/2019GC008515.

WOCE, 2002. World Ocean Circulation Experiment, Global Data, Version 3.0. WOCE International Project Office, WOCE Report, Southampton, UK; published by U.S. National Oceanographic Data Center, Silver Spring, 180/02, DVD-ROM. https://doi.org/10.1594/PANGAEA.737942

Wyrwoll, K.-H., Dong, B., Valdes, P., 2000. On the position of southern hemisphere westerlies at the Last Glacial Maximum: an outline of AGCM simulation results and evaluation of their implications. Quaternary Science Reviews 19, 881–898.

Figure 1: Maps of the Southern Ocean and of the Kerguelen Plateau region made with GMT v6 (Wessel et al., 2019) using the Etopo 1 min arc database (Amante and Eakins, 2008). The black square represents the location of MD11-3353 core site. White dots represent locations of core sites with published records used in this study. The main ACC fronts are drawn after Park et al. (2019). SAF: Subantarctic Front (red line); APF: Antarctic Polar Front (blue line); SACCF: Southern Antarctic Circumpolar Current Front (black line). Thin black lines represent contour lines between -8 and 8 km with a 0.5 km interval.

Figure 2: Age model of core MD11-3353. Tuning of the sub-STrad record (blue) with the δD EDC record (brown; Jouzel et al., 2007; Bazin et al., 2013). Yellow squares represent the tie points derived from the comparison of the TEX_L^{86} SST record (Thöle et al., 2019; supplementary table 1) and the δD EDC record (Jouzel et al., 2007) while sub-STrad derived tie points are represented by blue dots (supplementary material 1).

Figure 3: Ocean temperatures and key radiolarian species in core MD11-3353. (A) sub-STrad (black line) and (B) SSTdiat (green line). Represented in light blue are the relative abundances of radiolarian species associated to the AZ: (C) *Cycladophora davisiana*; (D) *Pseudodictyophimus gracilipes* gp; (E) *Botryostrobus auritus*; (F) *Lithomelissa* sp. A. Represented in dark blue (G) are the variations in relative abundances of the *Antarctissa*

group, associated with the APF. Represented in red are the variations in relative abundance of species associated to the north PFZ-SAZ: (H) *Cycladophora bicornis* and (I) *Lithomelissa setosa* gp. The range of depth in the water column where species live is represented above their relative abundance variations. Grey horizontal bars represent glacials, red bars represent peak-interglacials (pIG) and green bars represent mild-interglacials (mIG), all discussed in section 5. AZ: Antarctic Zone; APF: Antarctic Polar Front; SAZ: Subantarctic Zone; Holo: Holocene; HCO: Holocene Climate Optimum.

Figure 4: Box and Whiskers plots showing variations of SSTdiat (green boxes) and sub-STrad (blue boxes) during glacials (MIS 2-4; MIS 6; MIS 8; MIS 10), peak-interglacials (HCO; pIG-5; pIG-7; pIG-9) and mild-interglacials (Holocene; mIG-5; mIG-7; mIG-9). Black squares represent the mean temperatures for each period. The SSTdiat and sub-STrad values in the MD11-3353 core-top sample (5.5 °C and 2.7 °C, respectively), used as modern references in the discussion, are represented by red dashed lines.

Figure 5: Comparison of temperature records from the Kerguelen Plateau region over the past 360 kyrs. (A) sub-STrad record from core MD12-3396CQ (red line; Civel-Mazens et al., 2021); (B) TEX_L^{86} SST record from core MD11-3353 (grey line; Thöle et al., 2019); (C) SSTdiat record from core MD11-3353 (green line; this study); (D) sub-STrad record from core MD11-3353 (dark blue line; this study); (E) SSTdiat record from core MD84-551 (light blue line; Pichon et al., 1992); (F) δD record from EDC (brown line; Jouzel et al., 2007; Bazin et al., 2013).

Figure 6: Maps of the Kerguelen plateau region with interpreted front locations for (A) Glacials, (B) peak-Interglacials (pIGs) and (C) mild-Interglacials (mIGs). In the three maps, dashed lines represent the modern positions of the SAF (red), the APF (dark blue) and the SACCF (black) after Park et al. (2019). In (A), mean glacial positions of the APF and SACCF are represented by light blue and black plain lines, respectively. In (B), mean peak-interglacial positions of the APF and SAF are represented by light blue and red plain lines, respectively. In (C) mean positions of the APF and the SAF during the weaker mIGs (Holocene and mIG-7) are represented by light blue and red plain lines, respectively. SAF: Subantarctic Front; APF: Antarctic Polar Front; SACCF: Southern Antarctic Circumpolar Current Front.

Table 1: PCA results for species with factor loadings higher than |0.2| in one of the first 3 factors.

Species	PC 1 (61%)	PC 2 (24%)	PC 3 (5%)
Antarctissa gp	**0.75565**	0.51408	0.19807
Botryostrobus auritus/australis	-0.031163	0.056051	**-0.28376**
Cycladophora bicornis	-0.012451	**-0.20832**	**0.26294**
Cycladophora davisiana	**-0.64144**	**0.65725**	0.16712
Lithomelissa sp. A	0.045073	-0.11373	**-0.69023**
Lithomelissa setosa gp	-0.077533	**-0.47567**	**0.41163**
Pseudodictyophimus gracilipes gp	-0.021504	0.025118	**-0.30348**

Supplementary table 1: Tie points resulting from correlation between the TEX_L^{86}-derived SST record (yellow) or sub-STrad record (blue) in core MD11-3353 with the δD record in EDC ice core (Jouzel et al., 2007; Bazin et al., 2013).

Supplementary table 2: Factor loadings for the 81 taxa in the first three factors of the PCA.

Highlights

- New approach to estimate Southern Ocean fronts migrations in the past
- Comparison of sea-surface and subsurface temperature records over the last 360 kyrs
- APF positioned north of the Kerguelen Plateau during glacials
- APF located in the Fawn Trough during early warm interglacials
- Potential impact of ACC and associated fronts shifts on water column mixing

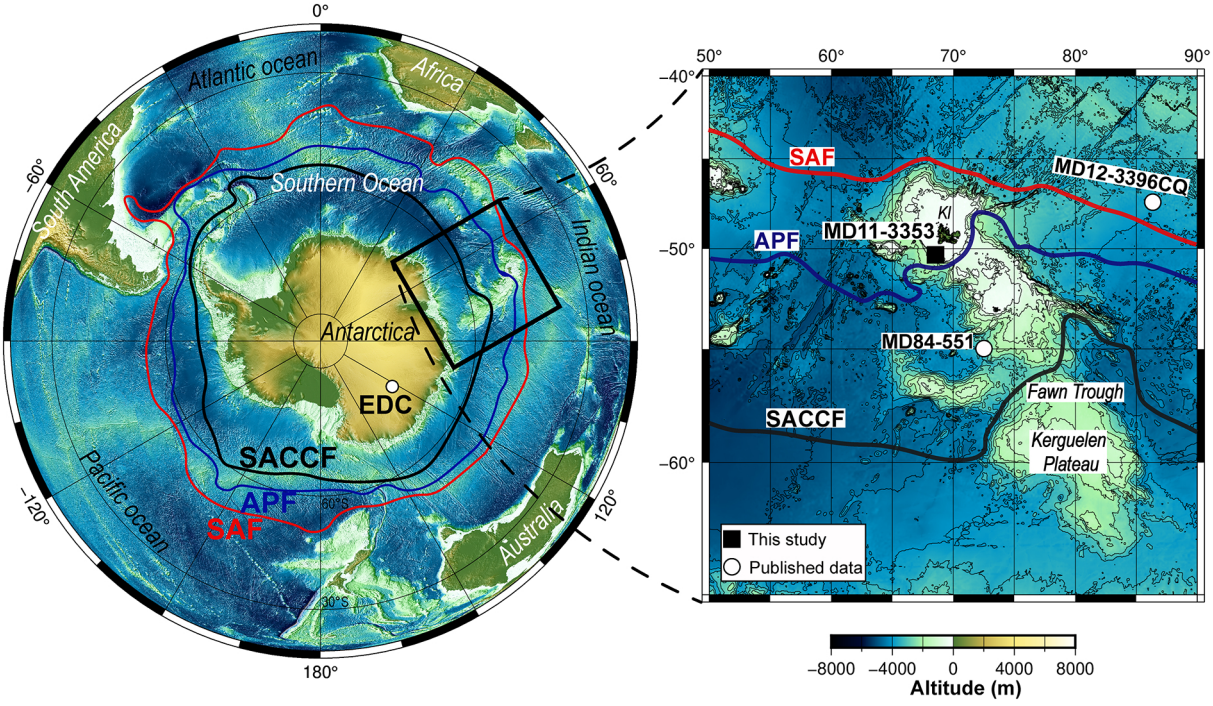
0°
Atlantic ocean
Africa
South America
Southern Ocean
60°
Indian ocean
Antarctica
EDC
SACCF
APF
SAF
Pacific ocean
120°
Australia
60°S
30°S
180°
50°
60°
70°
80°
90°
40°
50°
60°
SAF
MD12-3396CQ
KI
MD11-3353
APF
MD84-551
Fawn Trough
SACCF
Kerguelen
Plateau
This study
Published data
–8000
–4000
0
4000
8000
Altitude (m)

Figure 1

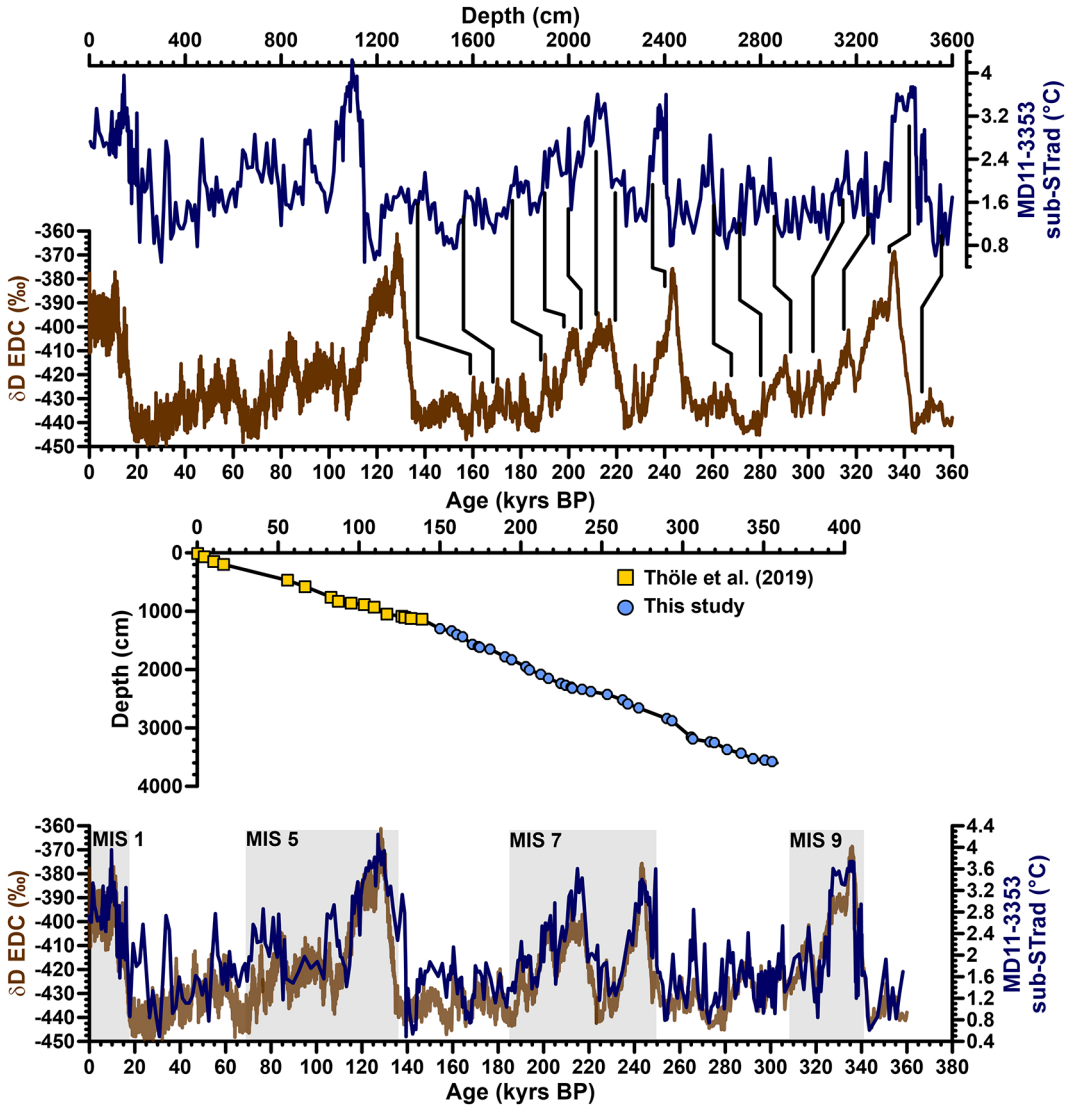
Depth (cm)
0 400 800 1200 1600 2000 2400 2800 3200 3600
4 3.2 2.4 1.6 0.8
MD11-3353 sub-STrad (°C)
δD EDC (‰)
-360 -370 -380 -390 -400 -410 -420 -430 -440 -450
0 20 40 60 80 100 120 140 160 180 200 220 240 260 280 300 320 340 360
Age (kyrs BP)
0 50 100 150 200 250 300 350 400
Depth (cm)
0 1000 2000 3000 4000
Thöle et al. (2019)
This study
MIS 1
MIS 5
MIS 7
MIS 9
δD EDC (‰)
-360 -370 -380 -390 -400 -410 -420 -430 -440 -450
4.4 4 3.6 3.2 2.8 2.4 2 1.6 1.2 0.8 0.4
MD11-3353 sub-STrad (°C)
0 20 40 60 80 100 120 140 160 180 200 220 240 260 280 300 320 340 360 380
Age (kyrs BP)

Figure 2

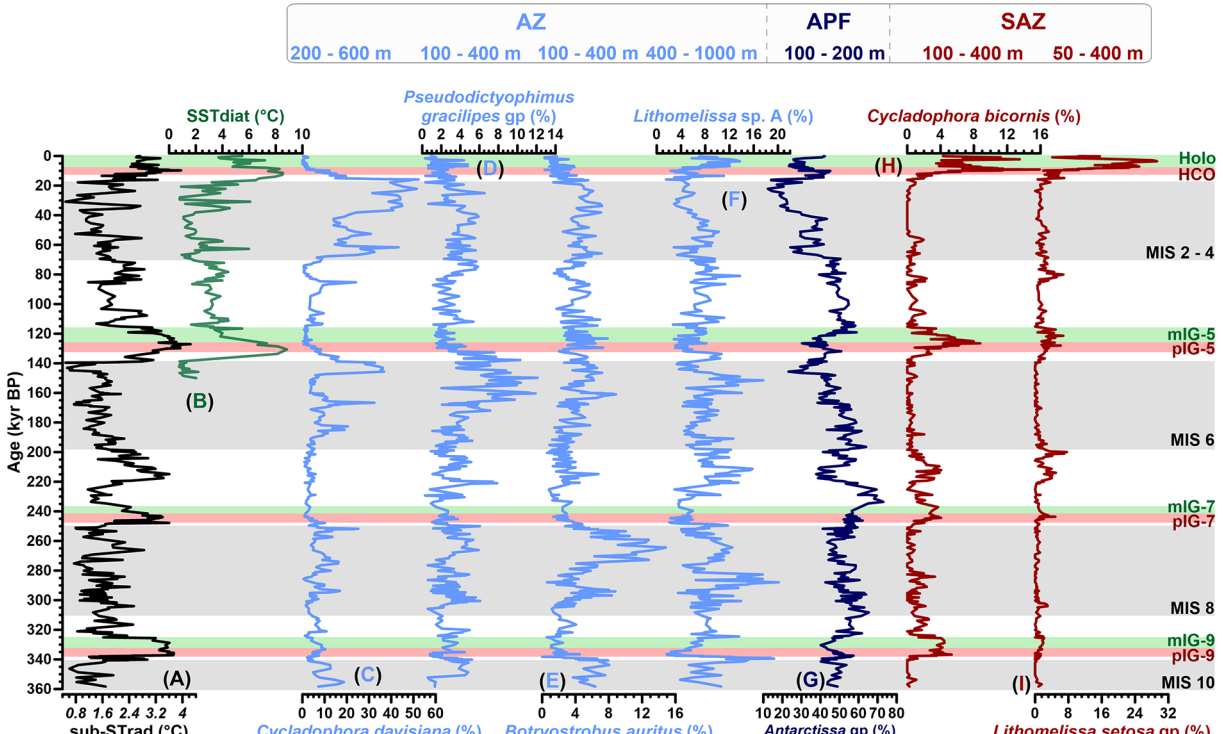
AZ
APF
SAZ
200 - 600 m
100 - 400 m
100 - 400 m
400 - 1000 m
100 - 200 m
100 - 400 m
50 - 400 m
SSTdiat (°C)
Pseudodictyophimus gracilipes gp (%)
Lithomelissa sp. A (%)
Cycladophora bicornis (%)
Holo
HCO
MIS 2 - 4
mIG-5
pIG-5
MIS 6
mIG-7
pIG-7
MIS 8
mIG-9
pIG-9
MIS 10
Age (kyr BP)
(A)
sub-STrad (°C)
(B)
(C)
Cycladophora davisiana (%)
(D)
(E)
Botryostrobus auritus (%)
(F)
(G)
Antarctissa gp (%)
(H)
(I)
Lithomelissa setosa gp (%)

Figure 3

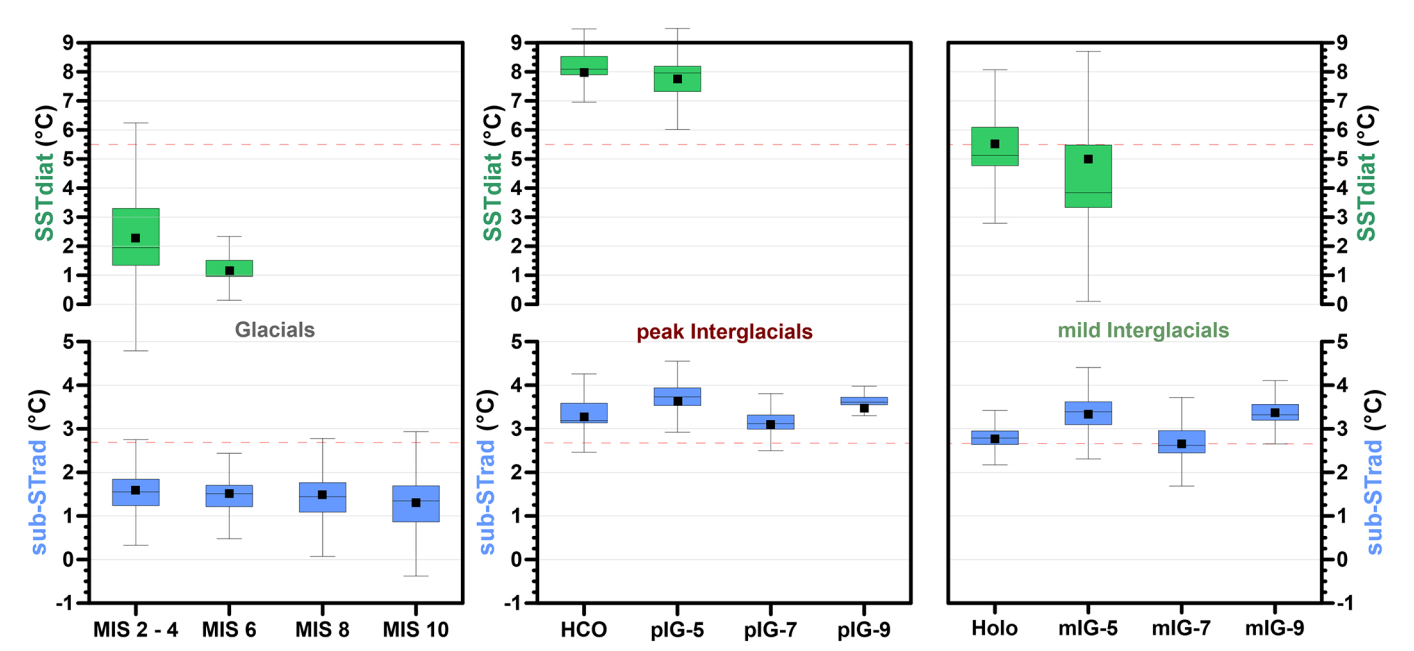
SSTdiat (°C)
sub-STrad (°C)
Glacials
peak Interglacials
mild Interglacials
MIS 2 - 4
MIS 6
MIS 8
MIS 10
HCO
pIG-5
pIG-7
pIG-9
Holo
mIG-5
mIG-7
mIG-9

Figure 4

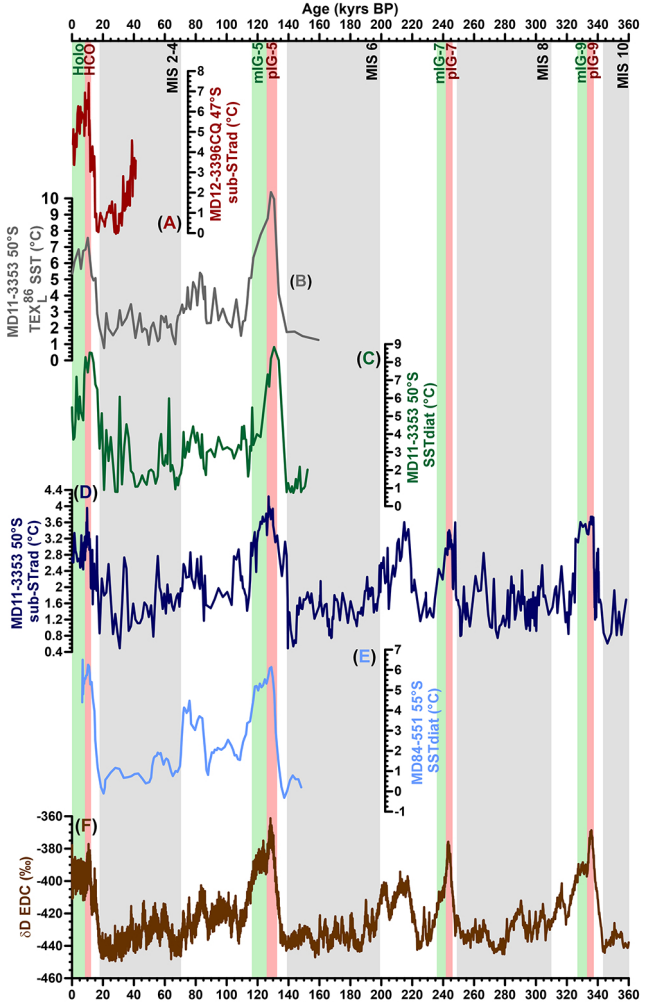
Age (kyrs BP)
Holo
HCO
MIS 2-4
mIG-5
pIG-5
MIS 6
mIG-7
pIG-7
MIS 8
mIG-9
pIG-9
MIS 10
(A)
MD12-3396CQ 47°S
sub-STrad (°C)
(B)
MD11-3353 50°S
TEX86L SST (°C)
(C)
MD11-3353 50°S
SSTdiat (°C)
(D)
MD11-3353 50°S
sub-STrad (°C)
(E)
MD84-551 55°S
SSTdiat (°C)
(F)
δD EDC (‰)
Age (kyrs BP)

Figure 5

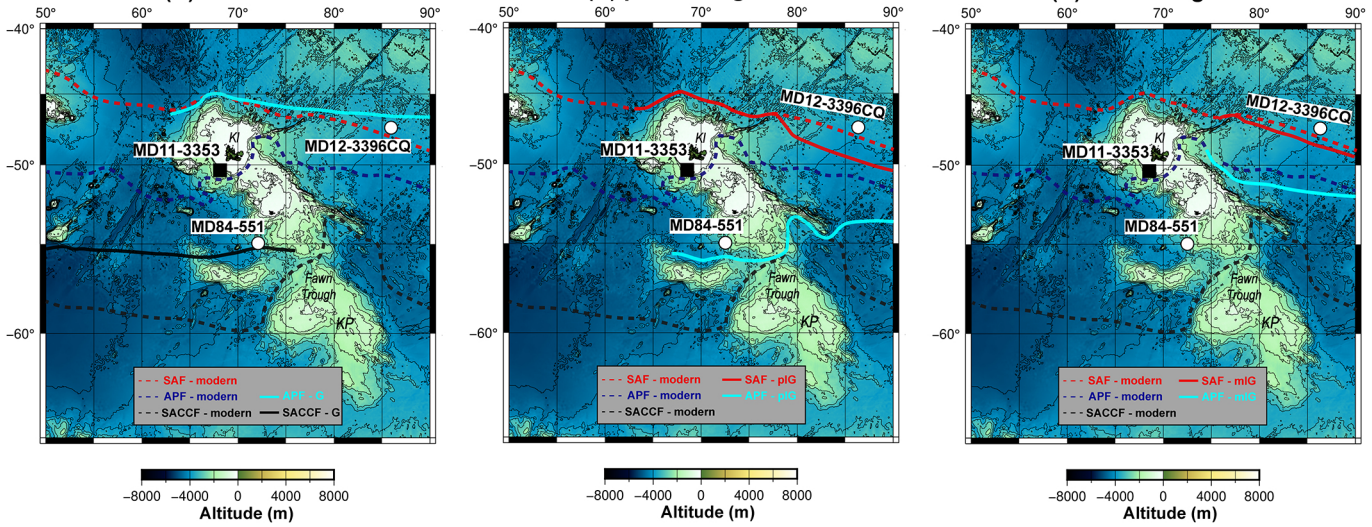
(A) Glacials
(B) peak-Interglacials
(C) mild-Interglacials
50°
60°
70°
80°
90°
−40°
−50°
−60°
MD11-3353
MD12-3396CQ
MD84-551
KI
KP
Fawn Trough
SAF - modern
APF - modern
SACCF - modern
APF - G
SACCF - G
SAF - pIG
APF - pIG
SAF - mIG
APF - mIG
−8000 −4000 0 4000 8000
Altitude (m)

Figure 6